Spatio-temporal dynamics of a periodically driven cavity flow

By M. J. VOGEL[1], A. H. HIRSA[1] AND J. M. LOPEZ[2]

[1]Department of Mechanical, Aerospace, and Nuclear Engineering, Rensselaer Polytechnic Institute, Troy, NY 12180, USA

[2]Department of Mathematics and Statistics, Arizona State University, Tempe, AZ 85287, USA

The flow in a rectangular cavity driven by the sinusoidal motion of the floor in its own plane has been studied both experimentally and computationally over a broad range of parameters. The stability limits of the time-periodic two-dimensional base state are of primary interest in the present study, as it is within these limits that the flow can be used as a viable surface viscometer (as outlined theoretically in Lopez & Hirsa 2001). Three flow regimes have been found experimentally in the parameter space considered: an essentially two-dimensional time-periodic flow, a time-periodic three-dimensional flow with a cellular structure in the spanwise direction, and a three-dimensional irregular (in both space and time) flow. The system poses a space–time symmetry that consists of a reflection about the vertical mid-plane together with a half-period translation in time (RT symmetry); the two-dimensional base state is invariant to this symmetry. Computations of the two-dimensional Navier–Stokes equations agree with experimentally measured velocity and vorticity to within experimental uncertainty in parameter regimes where the flow is essentially uniform in the spanwise direction, indicating that in this cavity with large spanwise aspect ratio, endwall effects are small and localized for these cases. Two classes of flows have been investigated, one with a rigid no-slip top and the other with a free surface. The basic states of these two cases are quite similar, but the free-surface case breaks RT symmetry at lower forcing amplitudes, and the structure of the three-dimensional states also differs significantly between the two classes.

1. Introduction

Studies to date on the lid-driven cavity have been focused on the steady driving case, where the lid moves at a constant velocity, and include both the flow in the steady state (for a recent comprehensive review, see Shankar & Deshpande 2000), as well as the start-up transients (e.g. Guermond *et al.* 2002). Recently, a new technique was introduced for measuring surface dilatational viscosity of a gas/liquid interface in the presence of insoluble monolayers (Lopez & Hirsa 2001) that requires flow in an oscillatory-driven cavity. The system, depicted in figure 1, consists of stationary streamwise sidewalls at $x = \pm \Gamma/2$, a floor at $y = 0$ moving periodically parallel to itself in the x-direction, and a nominally flat free surface at $y = 1$. In practice, the system is also bounded by spanwise endwalls at $z = \pm \Lambda/2$. It was shown by Lopez & Hirsa (2001) that for the system to be sensitive to interfacial viscosity, both the amplitude and the frequency of the floor oscillation had to be sufficiently large. Thus, for practical operation of the surface viscometer, the floor has to be
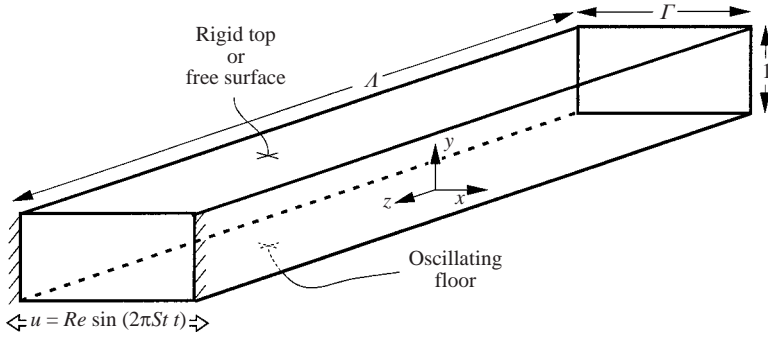
FIGURE 1. Schematic of the flow geometry.

driven relatively fast. The theory behind the design assumed two-dimensional flow, and so the stability limits of the bulk flow to three-dimensional disturbances in the oscillatory-driven cavity must be considered. It is expected that the bulk flow can become unstable through the roll-up of the shear layer turned into the interior by the sidewalls at $x = \pm \Gamma/2$, thus forming rollers that may be unstable to three-dimensional disturbances. Although the bulk flow shares some characteristics with the steady lid-driven cavity, the forcing makes the oscillatory-driven cavity fundamentally different.

While there is a very extensive body of literature on various aspects of the steady lid-driven cavity problem, for our present problem we are primarily interested in the manner in which the main roller loses stability, essentially in the absence of endwall effects (i.e. large Λ). The vast majority of past experiments have dealt with square cavities ($\Gamma = 1$) that are relatively short in the spanwise direction ($\Lambda \leqslant 3$). In these, the effects of the endwalls at $z = \pm\Lambda/2$ are quite pronounced, in much the same way that endwall effects are significant in Taylor–Couette flow in short annuli (e.g. Benjamin 1978). Linear stability analysis of the basic two-dimensional flow, of course, neglects such endwall effects. Early stability analysis of three-dimensional instability (e.g. Ramanan & Homsy 1994) suggests that the instability of the main roller is centrifugal in nature with a critical eigenmode reminiscent of Taylor–Görtler-like vortices, which were similar to earlier experimentally observed three-dimensional structures (e.g. Rhee, Koseff & Street 1984). Taylor–Görtler-like vortices were also found in three-dimensional computations in a square driven cavity with periodicity in the spanwise direction (Kim & Moin 1985). Albensoeder, Kuhlmann & Rath (2001) have recently presented a comprehensive linear stability analysis in more general rectangular cavities, as well as experiments in a relatively wide square cavity ($\Lambda \approx 6.55$). For shallow cavities (i.e. when the depth, which is the distance between the driven wall and the opposite stationary wall, is less than the separation between the streamwise sidewalls), they also describe a centrifugal instability of the roller that is Taylor–Görtler-like, and the structure and wavelength of the critical eigenmode compares well with the three-dimensional instability that they observe experimentally. In our oscillatory-driven cavity, we find that the rollers are also unstable to three-dimensional modes of similar structure, but the temporal forcing introduces different symmetries into the problem (in particular, it introduces a spatio-temporal symmetry), and these alter the nature of the bifurcations leading to instability of the basic state.

The oscillation of the floor relates our problem to Stokes' problem of an infinite plate oscillating harmonically in its own plane in a semi-infinite domain (Stokes 1851).

That problem has an exact similarity solution that describes an oscillatory (in both time and the normal direction) boundary layer whose thickness scales with the square root of the oscillation period. Von Kerczek & Davis (1972) have also obtained an exact solution for the modified problem where a second stationary parallel plate is placed at some distance from the oscillating plate. Both of these problems, of infinite horizontal extent, are linearly stable (von Kerczek & Davis 1974). These results however are not adequate to describe our problem, as the sidewalls at $x = \pm \Gamma/2$ play a major role. Even in the limit $\Gamma \to \infty$, their presence changes the problem as they impose a zero net mass flux condition. This means that on the opposite stationary plate there must be a return flow to conserve mass in the horizontally confined problem that sets up another oscillatory boundary layer flow at $y = 1$ (e.g. see Marques & Lopez 1997, for a discussion of this effect in a harmonically driven annular flow). Another effect of the sidewalls at $x = \pm \Gamma/2$ is that they roll up the Stokes layer, near $x = \Gamma/2$ on the positive stroke and $x = -\Gamma/2$ on the negative stroke, forming two rollers that are reminiscent of the roller in the steady lid-driven cavity flow. However, there are some important differences. The present rollers here are never at steady state. Before one is completely formed, the floor starts moving in the opposite direction. This tends to 'unroll' the roller while a new roller is formed at the opposite end.

Although studies on the stability of the present oscillatory-driven cavity flow have not previously appeared, several related studies have been published on oscillatory-driven cavities. O'Brien (1975a) considered the flow in small-depth cavities ($\Gamma \to \infty$); this limit results in a linear problem due to the parallel flow over most of the cavity. The effect of the pressure gradient produced by the sidewalls and the resulting oscillatory boundary layer on the wall opposite the sinusoidally driven wall was included in the analysis. The analytical results were favourably compared to visualizations of dye lines. A computational study of the nonlinear problem (finite Γ) was presented by O'Brien (1975b) for the cavity with two opposing walls co-moving sinusoidally. In both cases, O'Brien only considered the two-dimensional base state. Various types of oscillatory-driven cavities have also been used to study the Lagrangian mixing and chaotic advection properties of the two-dimensional basic state (e.g. Ottino 1997), but these studies were restricted to low driving amplitudes and did not investigate the flow stability. At the other extreme, coastal engineers have used the oscillatory-driven cavity as a model to investigate the dynamics of the coastal boundary layers (e.g. Bagnold 1946; Jonsson 1980; Sleath 1987; Krstic & Fernando 2001), usually with a rough oscillatory floor and driven at large amplitudes in order to simulate turbulence in the coastal layers.

Following a description of the experimental apparatus in the next section (§ 2), a discussion of the relevant symmetries is presented at the beginning of § 3. The subsections §§ 3.1–3.3 describe the three flow regimes that were observed for the rigid-top case. The location of those regimes in amplitude–frequency parameter space is summarized in § 3.4. Results for the free-surface case are presented in § 3.5, which is followed by the conclusions in § 4. Finally, details of the numerical technique are presented in the Appendix.

2. Experimental technique

The experiments were conducted in a periodically driven cavity with acrylic walls, illustrated in figure 2. The parts were machined to a tolerance of $\pm 0.003\,\text{cm}$. The depth of the channel was $H = 1\,\text{cm}$ and the streamwise width was $\Gamma H = 2\,\text{cm}$. The
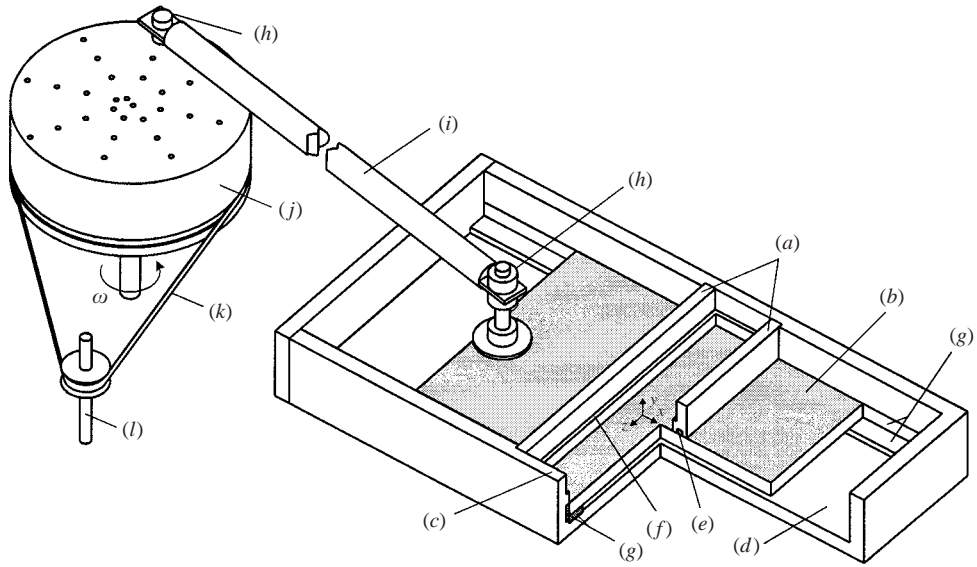
FIGURE 2. Schematic of the experimental apparatus. The letters indicate: (*a*) sidewalls at $x = \pm\Gamma/2$; (*b*) oscillatory glass floor; (*c*) endwalls at $z = \pm\Lambda/2$; (*d*) floor of the Plexiglas container; (*e*) dynamic seals; (*f*) free-surface groove and solid wall position at $y = 1$; (*g*) Teflon slide pads for oscillatory glass floor; (*h*) ball bearings; (*i*) connecting rod; (*j*) drive wheel; (*k*) drive belt; (*l*) stepper motor and belt pulley.

spanwise width of the channel was $\Lambda H = 19.4$ cm. The oscillatory floor was made of plate glass with a thickness of 1.17 cm, and was flat to ±0.002 cm. The relatively large thickness and consequently large mass of the floor was selected to reduce high-frequency vibrations. The oscillatory glass floor moved in machined grooves lined with Teflon with a tolerance of ±0.01 cm in the spanwise (z) direction.

In order to eliminate fluid transport in or out of the driven cavity, the bottoms of the sidewalls were sealed against the oscillatory glass floor. The dynamic seals were made of small-diameter Teflon tubes (0.318 cm outer diameter and 0.08 cm wall thickness) pressed inside grooves machined on the bottoms of the acrylic sidewalls. Teflon tubes with interference fit were also utilized as static seals at the ends of the sidewalls where they met the endwalls. For the free-surface case, the contact line was fixed by grooves machined on the inside of each sidewall, similar to those in Hirsa, Lopez & Miraghaie (2001*a*). For the rigid-top case, a glass cover was fitted inside the grooves in the sidewalls.

The oscillatory motion of the floor was accomplished with a drive wheel and connecting rod assembly, as depicted in figure 2. The amplitude of the floor motion was set by the radius at which the connecting rod was attached to the drive wheel. Precision ball bearings were used for attaching each end of the connecting rod as well as supporting the drive wheel. The drive wheel, machined from aluminium, had a diameter of 15.2 cm and a thickness of 6.9 cm. A steel flywheel, with a diameter of 16.5 cm and thickness of 2.4 cm was attached to the same shaft as the drive wheel to make its motion smooth. A computer-controlled stepper motor was utilized to turn the drive wheel. A drive belt and pulley assembly with a 5:1 speed ratio (motor to drive wheel) was utilized to reduce vibrations at the drive wheel caused by the motor. A separate flywheel (16.5 cm diameter and 2 cm in thickness, also made of

steel) was utilized on the motor to reduce its vibrations. Furthermore, microstepping of the motor (25 000 microsteps per motor revolution) helped to smooth the motion of the drive wheel. It should be noted that the length of the connecting rod (94 cm) was chosen to be large compared to the stroke length ($\leqslant 14$ cm) to minimize the departure of the floor motion from an exact sine wave. The r.m.s. of this variation from sinusoidal motion ranged from 0.4% to 1.5% for the range of parameters for which direct comparisons to computations were made. The difference between the actual motion and an exact sine wave may become important in the neighbourhood of symmetry-breaking bifurcations, but away from these this difference is not detectable, as it is less than the uncertainty in the velocity measurements. Using H as the length scale and the viscous time across the depth of the cavity, H^2/ν (ν is the kinematic viscosity of water; $\nu = 0.00957$ cm^2 s^{-1} for water which was maintained at $22 \pm 0.5°$C), as the time scale, the velocity of the floor is given by

$$(u, v, w) = (Re \sin(2\pi St\, t), 0, 0),$$

where the Reynolds number

$$Re = U_{\mathrm{max}} H/\nu$$

is the scaled amplitude (U_{max} cm s^{-1} is the maximum speed of the floor), and the Stokes number

$$St = \omega H^2/\nu$$

is the scaled frequency (ω rad s^{-1} is the frequency of the floor).

Although both the stepper motor and the data acquisition system were operated by digital circuits, extremely small variations in their clock speeds could cause an error in the phase over the duration of each experiment, some of which lasted hundreds of cycles. In order to ensure that the motion of the oscillatory floor was completely synchronized with the data acquisition system, an algorithm was developed to make fine adjustments to the speed of the stepper motor. The adjustments to the speed were always less than one part in 10^4 and were usually less than one part in 10^5 for the entire duration of each experiment. Thus, the variations in Re and St due to motor speed changes over the course of an experiment were less than one part in 10^4.

The range of parameters, Re and St, that the experimental apparatus could be operated at was limited by the maximum stroke length of the floor. Since $L\pi St = H Re$, where L is the stroke length, the present channel with $H = 1$ cm and a maximum stroke length of 15 cm could not be operated with $Re > 15\pi St$. Also, limitations on the speed of the stepper-motor controller precluded operation at St larger than about 53 for the present conditions (i.e. for the given H and ν).

Double-distilled water was used in the experiments. For measurements with the digital particle image velocimetry (DPIV) system, the water was seeded with 21 μm particles (Duke Scientific, 7520A). Details of the procedure for cleaning particles, as well as references to the present DPIV system, can be found in Hirsa *et al.* (2001*a*). Additional details of the present experiments are available in Vogel (2002).

3. Results

The basic flow state will have the symmetries of the system. The geometry is a rectangular box, but the system does not have the symmetry of a rectangular box due to the periodic oscillation of the floor. The only spatial invariance is reflection about $z = 0$:

$$(u, v, w)(x, y, z, t) = (u, v, -w)(x, y, -z, t),$$

i.e. Z_2 symmetry. However, in the limit $\Lambda \to \infty$, the spatial invariances are reflection about any (x, y)-plane and arbitrary translations in the spanwise z-direction, leading to $O(2)$ symmetry. This is analogous to the situation in Taylor–Couette flow where, for finite cylinders there is reflection invariance about the annulus half-height (Z_2 symmetry), and in the limit of infinitely long cylinders there is invariance to reflection about any height and arbitrary translations along the annulus ($O(2)$ symmetry). The harmonic oscillation of the floor in our cavity introduces a spatio-temporal invariance. The system is invariant to a reflection about $x = 0$ together with a half-period translation in time:

$$(u, v, w)(x, y, z, t) = (-u, v, w)(-x, y, z, t + T/2),$$

where $T = 1/St$ is the period of the floor oscillation. This temporal glide-reflection symmetry, which we shall denote as RT symmetry, is isomorphic to Z_2. So the complete symmetry group of our finite oscillatory cavity is $Z_2 \times Z_2$. For any finite oscillatory cavity, the basic state is three-dimensional and time-periodic, synchronous with the oscillation of the floor. For sufficiently large Λ (i.e. spanwise endwalls sufficiently far apart), the basic state away from the endwalls ($z = \pm\Lambda/2$) may be expected to be approximated by a two-dimensional state (independent of z), as in the case of Taylor–Couette flow. In Taylor–Couette flow, many of the characteristics of the first few instability modes observed in physical experiments can be accounted for by normal-form theory based on $O(2)$ equivariance (e.g. see Chossat & Iooss 1994).

The basic state can be expected to become unstable via symmetry-breaking bifurcations. If the cavity were two-dimensional ($\Lambda \to \infty$), then the $O(2)$ symmetry breaking could be expected to lead to cellular structures with spatially periodic variation in the z-direction. Since our finite cavity replaces the $O(2)$ symmetry of the ideal infinite case with the spatial Z_2, we should expect a smooth transition from approximately two-dimensional flow to cellular-type flow, following the characteristics of an imperfect pitchfork bifurcation. The symmetry-breaking bifurcations of the two-dimensional time-periodic basic state will follow the equivariant branching lemma (e.g. see Golubitsky, Stewart & Schaeffer 1988; Chossat & Lauterbach 2000); for additional details associated with RT symmetry, see Lamb & Melbourne (1999a,b).

The time-periodic nature of the base flow may lose stability in a number of ways. One is via a synchronous bifurcation, whereby a Floquet multiplier crosses the unit circle at $+1$, and another time-periodic state synchronous with the floor oscillation results (breaking of the spatial Z_2 symmetry would be such an example). Another possibility is for a pair of complex conjugate multipliers to cross the unit circle, giving rise to a quasi-periodic state, one frequency corresponding to the frequency of the floor oscillation and the other to the imaginary part of the critical Floquet multipliers that attain unit modulus at the Neimark–Sacker bifurcation. The third generic way that a time-periodic flow may lose stability is via a period-doubling bifurcation, whereby the critical Floquet multiplier crosses the unit circle at -1 (Kuznetsov 1998). This third scenario, however, is prohibited for our basic state due to the spatio-temporal Z_2 (RT) symmetry. The Poincaré map (i.e. strobing at the frequency of the floor oscillation) for our symmetric system is the square of another map (strobing at twice the frequency together with a reflection about $x = 0$), inhibiting period doubling via a simple eigenvalue -1 (Swift & Wiesenfeld 1984; Marques & Lopez 2000). In this section, we shall explore to what extent these considerations are fulfilled in our finite $1 : \Gamma : \Lambda = 1 : 2 : 19$ oscillatory cavity.

FIGURE 3. Instantaneous photo of dye streaks approximately two periods after start-up for a case with $Re = 747$ and $St = 53$. The image was taken looking from above, showing $x \in [-\Gamma/2, \Gamma/2]$ and $z \in [-0.9\Lambda/2, 0.9\Lambda/2]$, so that only a small portion of the cavity near the two endwalls is missing from the field of view. Dye (dark) was initially injected along the sidewall, $x = -\Gamma/2$, seen at the bottom of the photograph, and was carried toward the top by the initial motion of the floor.
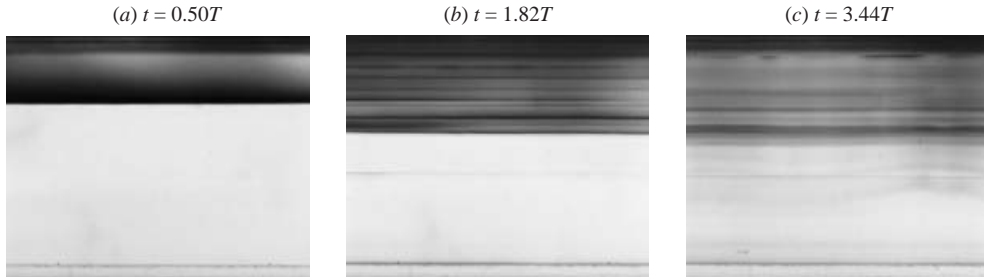
| (a) $t = 0.50T$ | (b) $t = 1.82T$ | (c) $t = 3.44T$ |

FIGURE 4. Temporal development of the case presented in figure 3, $Re = 747$ and $St = 53$, showing the central portion of the cavity, looking from above near $z = 0$, at times following start-up as indicated, T being the period of the floor oscillation. Note that (dark) dye was initially injected along the bottom of each photograph.

3.1. *Basic state with a rigid top*

Flow visualizations using dye were first performed along the entire channel in order to establish the spanwise influence of the endwalls. The visualizations with dye were accomplished by injecting a small volume of (diluted) food colouring along the bottom edge of one sidewall using a 100 µl (0.1 ml) syringe. Approximately 0.08 ml (or 0.002 times the cavity volume) of dye was deposited along the entire length of one sidewall, which gradually sunk to the floor due to its slightly larger than unity specific gravity. The oscillatory floor was started once the fluid motion resulting from the dye injection process had diminished. The pictures were taken with a CCD digital camera.

Figure 3 shows the dye streaks along nearly the entire span of the cavity. In every photograph shown in this paper, the (dark) dye was injected along the bottom of the picture ($x = -\Gamma/2$) and the initial motion of the floor was towards the top of the photograph. The motion during the first half of the cycle is responsible for carrying most of the dye toward the top of each photograph ($x = \Gamma/2$). The picture in figure 3 shows that the flow is stable to three-dimensional disturbances, as there is little variation in the z-direction, even though there were, inevitably, some non-uniformities in the initial distribution of the dye. The slightly brighter region at about 1/3 of the span from the right side of the photo is due to non-uniformity in illumination and is not related to the flow. Also, the slightly darker, small, wavy streak at about 1/10 of the span from the left side of the photo is due to imperfections on the bottom side of the glass oscillatory floor, i.e. on the outside of the cavity and so these do not affect the flow. Figure 3 shows that after two periods ($2T$) following the start-up, the flow at $Re = 747$ and $St = 53$ is remarkably two-dimensional over nearly the entire span of the cavity.

The development of the dye streaks for a different realization of the same flow is shown in the close-up pictures (centred about $z = 0$) in figure 4. One sidewall is

visible near the top and the other near the bottom of each picture. The sequence shows that the flow remains essentially two-dimensional over several periods of the floor. Due to dye diffusion and mixing, it is difficult to visualize the flow after only a few periods, so the velocity field was measured using DPIV both in cross-sectional planes (z =constant) as well as horizontal planes (y =constant) over several hundred periods and there were no z-variations at these parameter values.

The dynamics of the flow for a relatively high Reynolds number case ($Re = 747$ and $St = 53$) as measured by DPIV are shown in figures 5 and 6. Figure 5 shows the instantaneous velocity at 10 phases during one period of floor oscillation. This measurement, obtained at the centre-plane ($z = 0$) long after the initial start-up transients had diminished, is identical to measurements obtained in other planes away from the endwalls, to within the experimental uncertainty ($\pm 2\%$ of maximum for velocity and $\pm 5\%$ for vorticity).

At the first phase shown ($t = NT$, where N is an integer $\gg 1$), the floor is about to start moving to the right but the vortex on the left side, produced when the floor was moving to the left in the previous cycle, is stronger than the right vortex. Figure 5 shows that during the first half of the cycle (until $t = 0.5T$) the right vortex is strengthened as fluid is forced to the right along the floor and then turned up by the right sidewall and subsequently turned toward the floor by the top wall and the left roller. The reverse occurs during the second half of the cycle. The generation of vorticity on the floor and its subsequent roll-up into the two rollers is demonstrated in figure 6. The two figures show that the remnant of each roller interacts with the bottom boundary layer and distorts the secondary vorticity on the sidewall as it is pulled into the interior by the new rollers. Thus, the remnant vortex is annihilated partially by the opposite-signed vorticity and its remainder merges with the new roller. Although a single cycle is shown in these figures, the flow is periodic and no cycle-to-cycle variations were detected. Thus, the flow is synchronous with the forcing and RT symmetry is observed in both the velocity and the vorticity data (compare the reflectional symmetry between the left and right columns, which are half a period apart).

Good agreement is obtained between the measured vorticity field (figure 6) and two-dimensional computations at the same Re, St and Γ, presented in figure 7. The computations were performed using a standard finite difference approach, utilizing the streamfunction–vorticity formulation. A brief description of the technique is presented in the Appendix. Identical contour levels, spaced quadratically, were used for both the experimentally and computationally determined z-component of vorticity shown in figures 6 and 7, respectively. These figures illustrate that all the large features are fully captured by the two-dimensional computations, including the peak vorticity level in each roller. The computations are advantageous in showing the flow features near boundaries, due to fundamental limitations in DPIV measurements in near-wall regions. However, away from the boundaries the agreement is within the experimental uncertainty. Based on these figures, we can conclude that the basic flow state (two-dimensional and periodic) is maintained up to and including these Reynolds numbers, and that three-dimensional effects due to the spanwise walls at $z = \pm \Lambda/2$ are small, at a level comparable to the uncertainty in the DPIV measurements.

At much lower Re (at the same $St = 53$), the rollers observed at $Re = 747$ do not form. Figure 8 shows a computed two-dimensional solution at $Re = 166$, where there is still a hint of the roller formations. Even though $\Gamma = 2$ is quite small, away from the sidewalls at $x = \pm \Gamma/2$ the flow is essentially independent of x, and has many characteristics of the flows considered by O'Brien (1975a) in the parallel
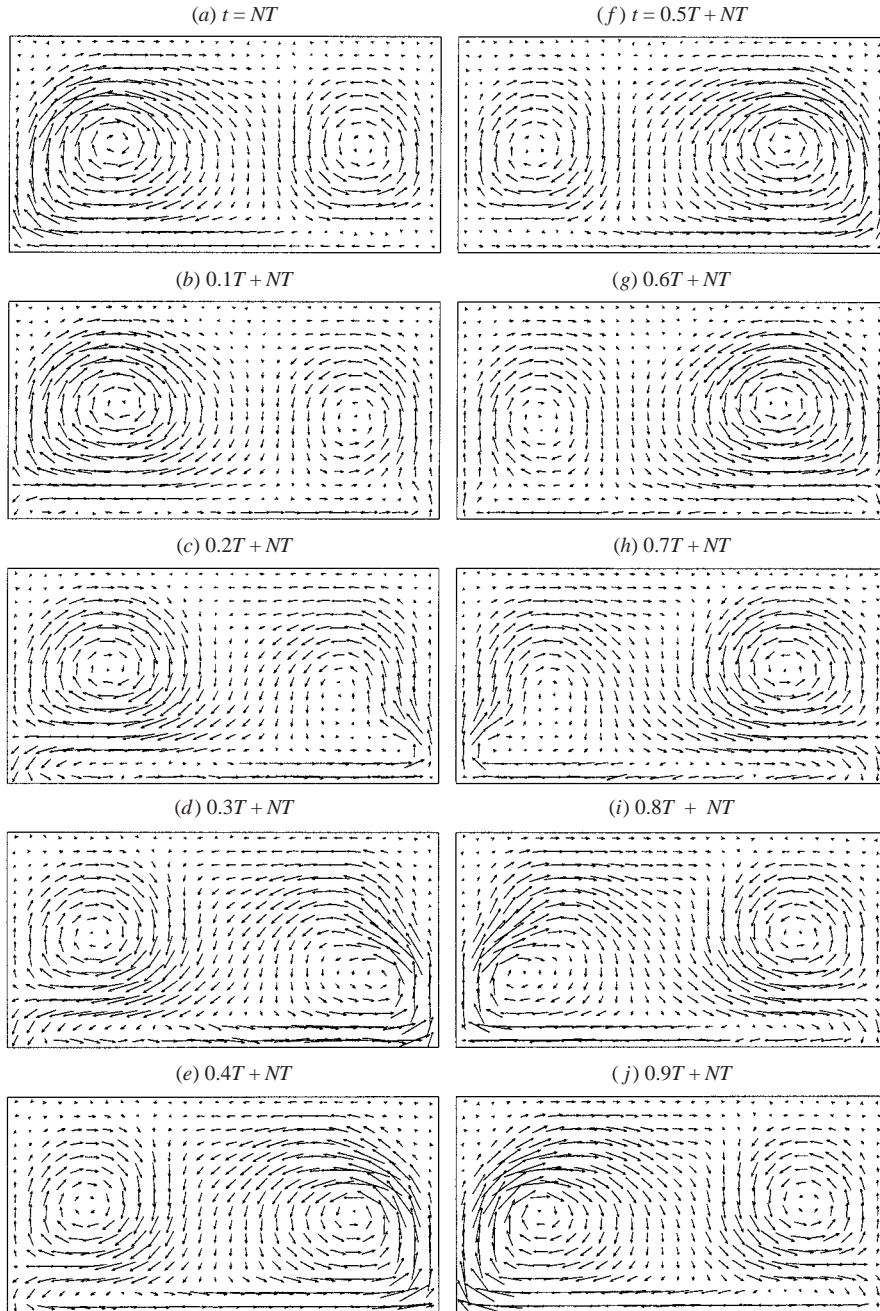
FIGURE 5. Velocity vectors (from experiment) in the $z = 0$ plane at ten phases over one period of the floor oscillation for the rigid top case at $Re = 747$, $St = 53$. Measurements were taken after the start-up transients had diminished following N periods (where N is a large integer).

flow limit, $\Gamma \to \infty$. The formation of the oscillatory Stokes layer is clearly evident on the oscillating floor, as is the oscillatory shear layer on the stationary rigid top boundary that forms in response to the zero net mass flux imposed by the sidewalls at $x = \pm\Gamma/2$.

(*a*) $t = NT$ (*f*) $t = 0.5T + NT$

(*b*) $0.1T + NT$ (*g*) $0.6T + NT$

(*c*) $0.2T + NT$ (*h*) $0.7T + NT$

(*d*) $0.3T + NT$ (*i*) $0.8T + NT$
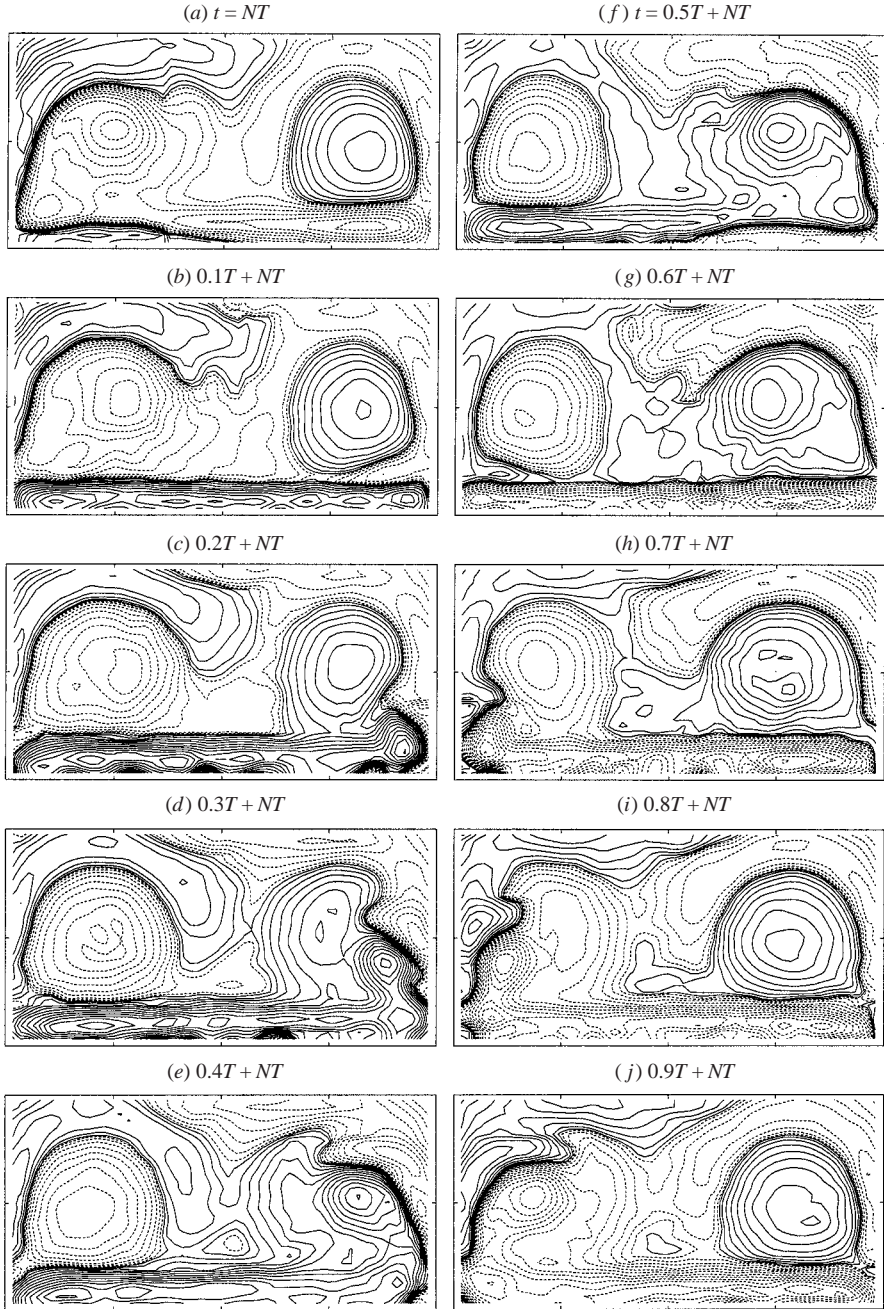
(*e*) $0.4T + NT$ (*j*) $0.9T + NT$

FIGURE 6. Contours of z-vorticity (from experiment) in the $z = 0$ plane at ten phases over one period of the floor oscillation for the rigid top case at $Re = 747$, $St = 53$. Solid curves correspond to positive values of vorticity. Measurements were taken after the start-up transients had diminished following N periods (where N is a large integer).

A parametric study of the base flow was performed by varying Re and St. Figure 9 presents measurements and computations performed at various Re for a fixed $St = 53$. The data shown in this figure are at a fixed phase ($t - NT = 0$). Good agreement is again found between the measurements and the computations, in the light of the
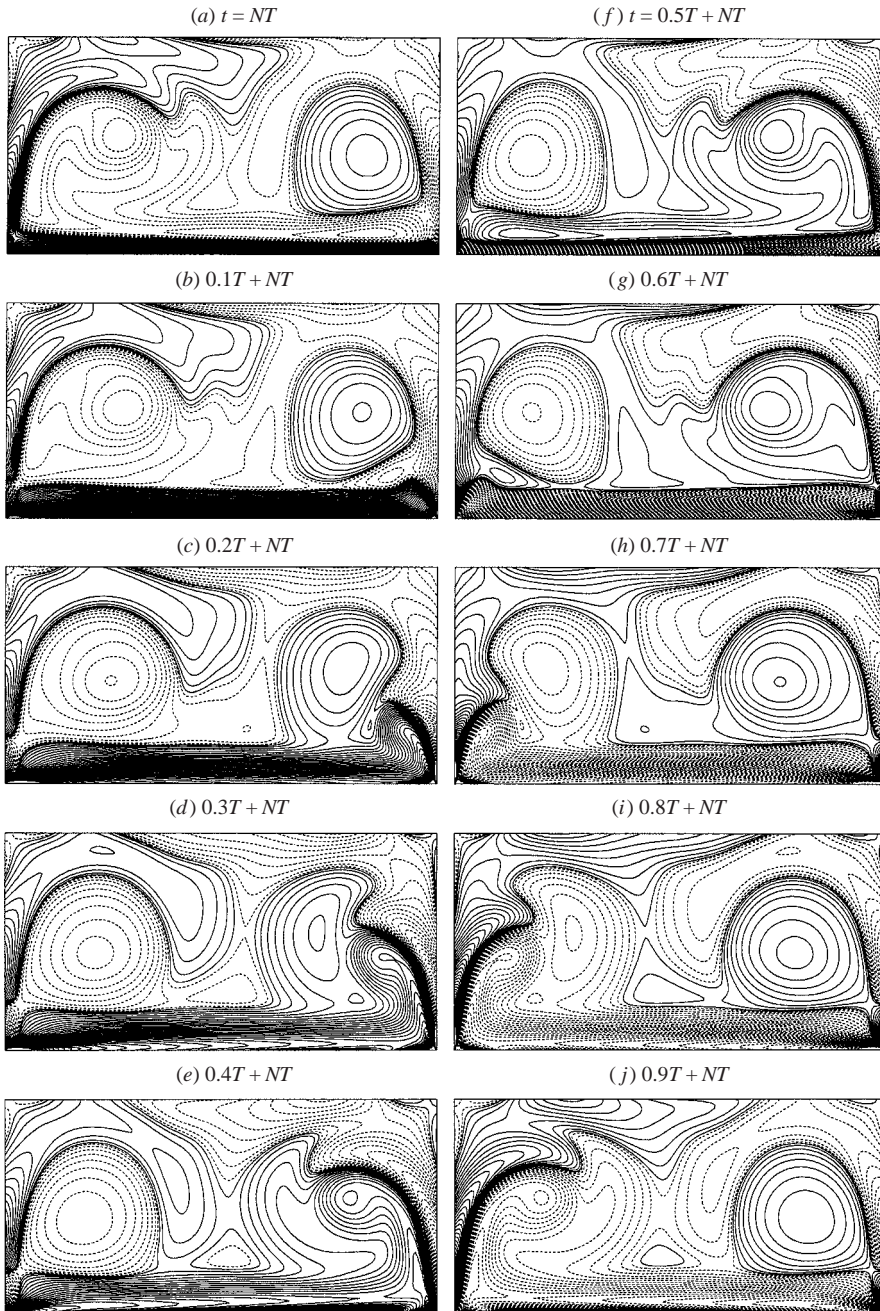
FIGURE 7. Contours of z-vorticity (from two-dimensional computations) at ten phases over one period of the floor oscillation for the rigid top case at $Re = 747$, $St = 53$. Results are shown after the start-up transients had diminished following N periods (where N is a large integer).

experimental uncertainty. The figure shows that at the lowest Re shown, the vorticity from the floor fails to roll up. As Re is increased, rollers form and become stronger. The positions of the rollers move up with increasing Re, but are eventually limited by the vorticity at the rigid top. This secondary vorticity, formed along the sidewalls
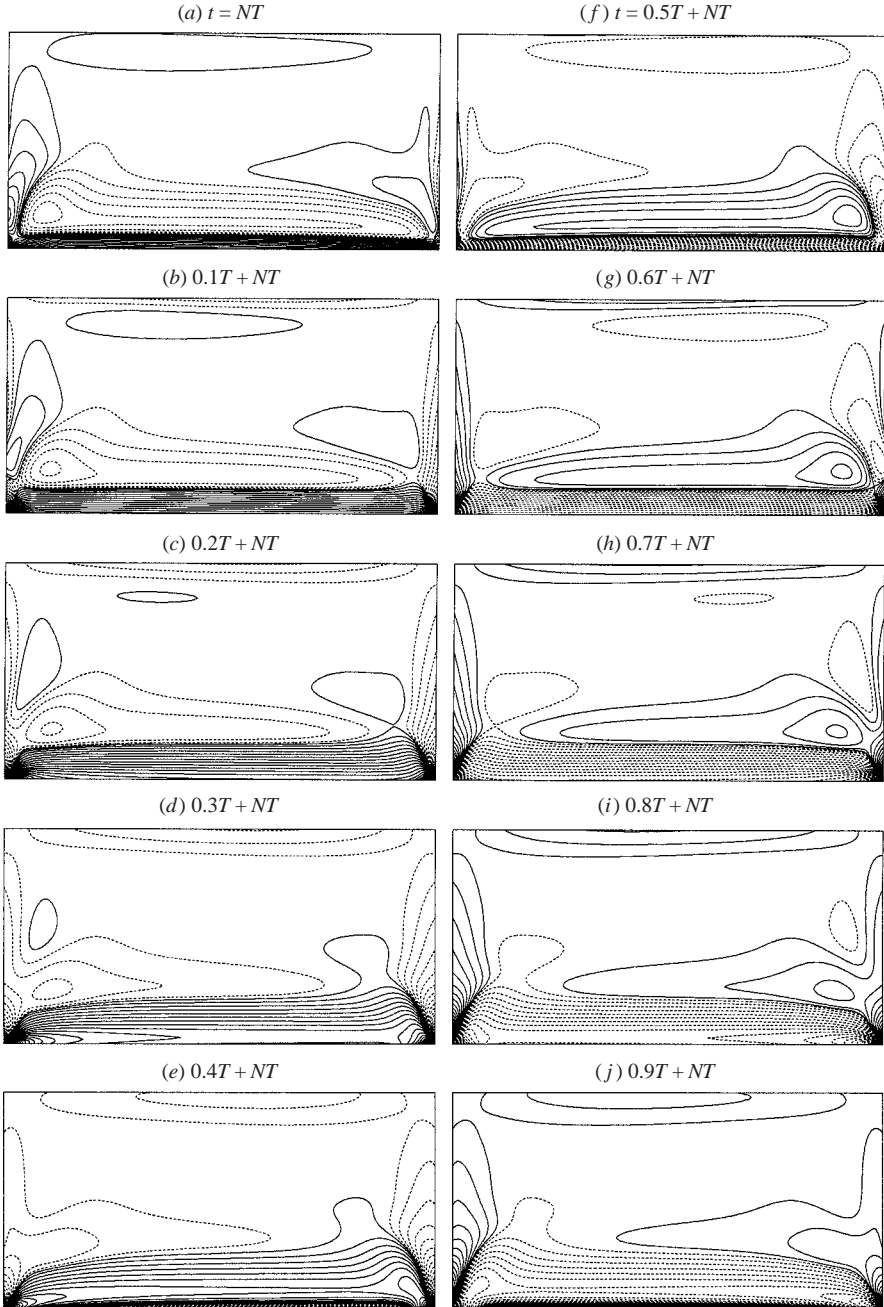
(*a*) $t = NT$

(*f*) $t = 0.5T + NT$

(*b*) $0.1T + NT$

(*g*) $0.6T + NT$

(*c*) $0.2T + NT$

(*h*) $0.7T + NT$

(*d*) $0.3T + NT$

(*i*) $0.8T + NT$

(*e*) $0.4T + NT$

(*j*) $0.9T + NT$

FIGURE 8. Contours of z-vorticity (from two-dimensional computations) at ten phases over one period of the floor oscillation for a rigid top at $Re = 166$, $St = 53$. Results are shown after the start-up transients had diminished following N periods (where N is a large integer).

as well as at the rigid top, is generated by the rollers. As Re increases, this secondary vorticity interacts more with the secondary vorticity generated by the opposing roller. Additionally, tertiary vorticity at the upper-left corner, generated by the secondary vorticity, is also observed at this phase.
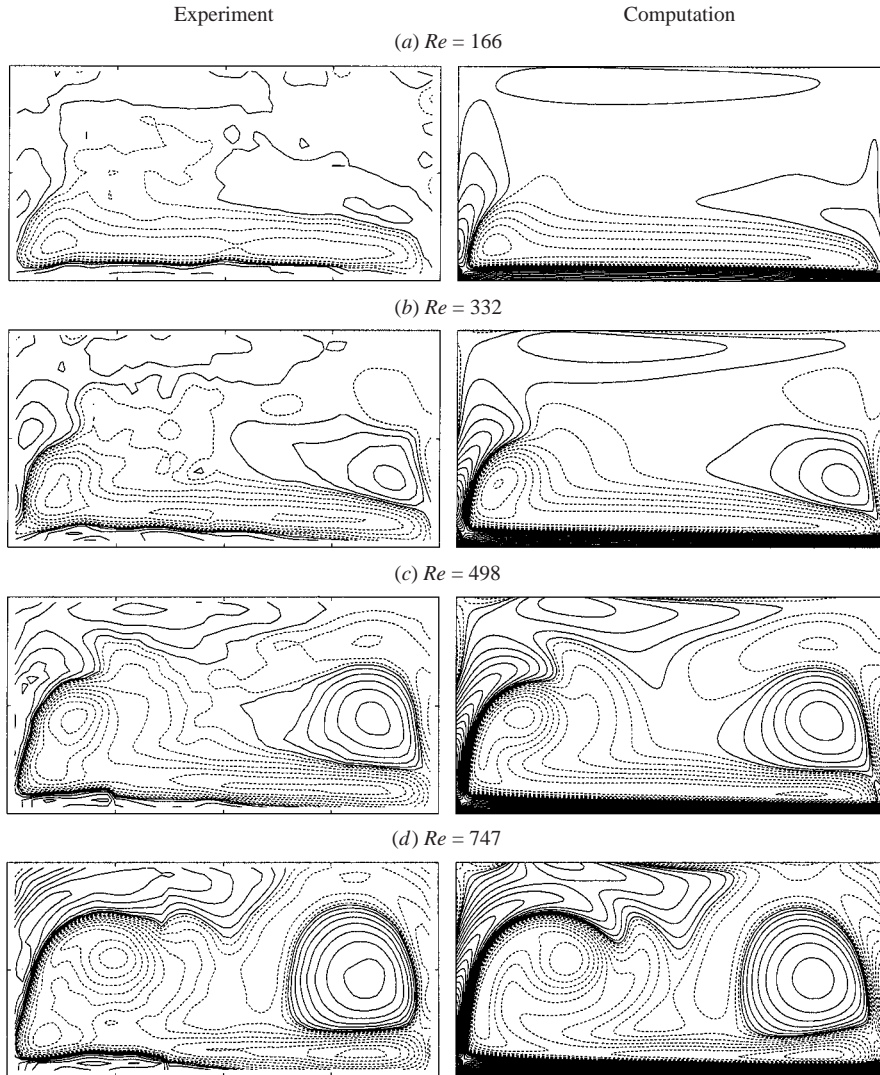
Experiment Computation

(*a*) *Re* = 166

(*b*) *Re* = 332

(*c*) *Re* = 498

(*d*) *Re* = 747

FIGURE 9. Measurements and two-dimensional computation of z-vorticity at various *Re* with fixed $St = 53$ for the rigid top case. All the data are for the phase $t - NT = 0$ (where N is a large integer) and utilize identical contouring levels.

The effects of varying *St* are presented in figure 10. The figure shows that as *St* is approximately doubled, from 20 to 39, the peak vorticity in the main roller (on the left at this phase) is increased, whereas the roller appears smaller. With increased *St*, the stroke length of the floor is decreased to keep *Re* constant, which subsequently decreases the circulation associated with each roller. Also, less negative vorticity is generated at the top wall and the positive vorticity generated at the left wall does not have sufficient time to merge with the right roller. Furthermore, the boundary layer on the floor thins slightly with increase in *St* (consistent with the Stokes scaling).

3.2. *Instability of the basic state with a rigid top: three-dimensional cellular flow*

When *Re* is increased beyond a critical value (and this value is a weak function of *St*), the essentially two-dimensional basic state undergoes a symmetry-breaking
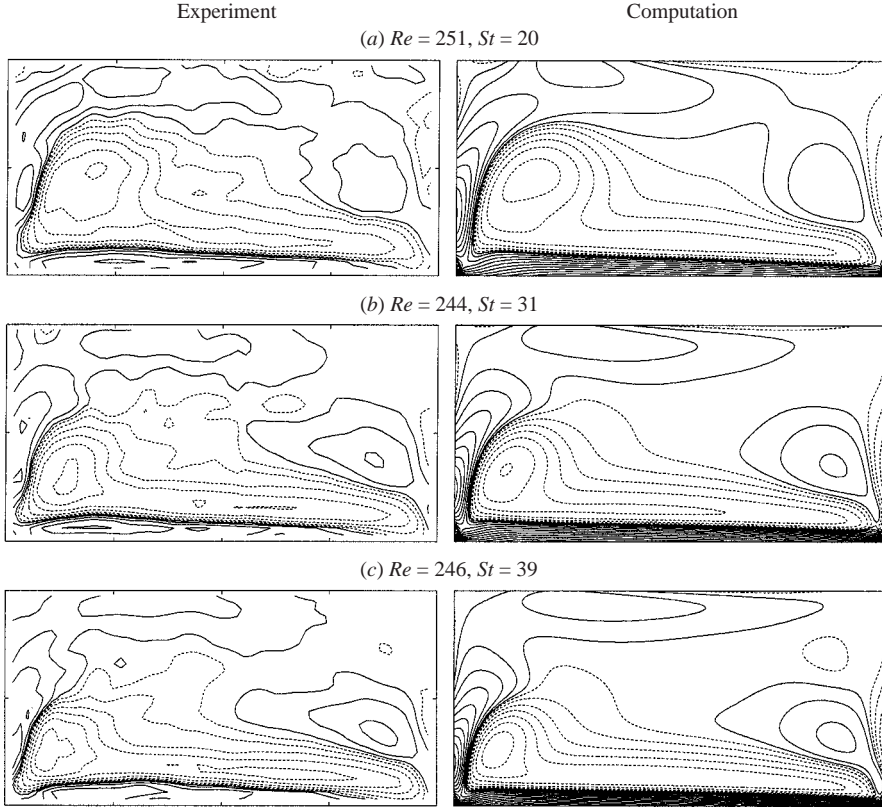
Experiment   Computation

(*a*) *Re* = 251, *St* = 20

(*b*) *Re* = 244, *St* = 31

(*c*) *Re* = 246, *St* = 39

FIGURE 10. Measurements and two-dimensional computation of *z*-vorticity at various *St* with nominally constant $Re \approx 250$ for the rigid top case. All the data are for the phase $t - NT = 0$ (where N is a large integer) and utilize identical contouring levels.

FIGURE 11. Instantaneous photo of dye streaks approximately two periods after start-up for the $Re = 1163$ and $St = 53$. The image was taken looking from above, showing $x \in [-\Gamma/2, \Gamma/2]$ and $z \in [-0.9\Lambda/2, 0.9\Lambda/2]$, so that only a small portion of the cavity near the two endwalls is missing from the field of view. Dye (dark) was initially deposited along the bottom of the photo.

bifurcation leading to a three-dimensional state whose most striking characteristic is a periodic cellular structure in the *z*-direction. Figure 11 is a photograph of (almost) the entire span of the cavity showing the dye streaks delineating the cellular structures for $Re = 1163$ and $St = 53$, after approximately two periods of the floor oscillation. Taking into account visual effects due to non-uniform lighting and initial dye distribution, the figure illustrates the regularity of the cellular structures across the span of the cavity.

In figure 12, close-up photographs at various times, for a different realization from figure 11 but for the same parameters, give an indication of the temporal development of the cellular structures. Figure 12 illustrates that even at the earliest time, evidence of three-dimensional flow is faintly detectable; compare the dye-front in figures 12(*a*)
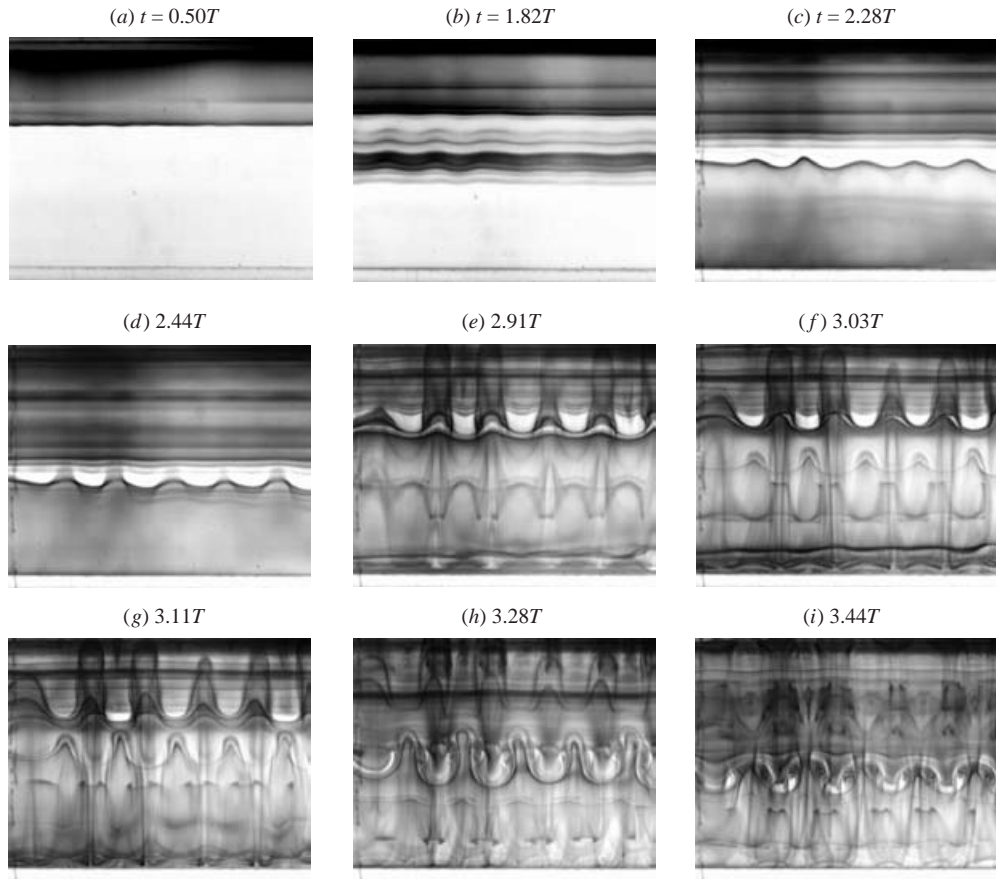
FIGURE 12. Temporal development of the case shown in figure 11, $Re = 1163$ and $St = 53$, showing on the central portion of the cavity, looking from above near $z = 0$, at times following start-up as indicated. Dye (dark) was initially injected along the bottom of each photograph.

and 4(a). The waviness in the dye increases and becomes significant after about $2T$. Cellular structures and associated cross-axis vortices become visible by $3T$. By about $3.5T$, a row of mushroom-shaped structures, formed by counter-rotating vortices, is visible. Visualization of unsteady flow with dye makes the interpretation of flow patterns difficult (Hama 1962). Also, flow visualization with dye does not provide any direct information about the structure of the flow in the depth-wise direction.

In order to quantify the cellular structures observed in the flow visualizations, DPIV measurements were performed in the (x, z)-plane at mid-depth ($y = 0.5$). Figure 13 shows the velocity vectors, (u, w), in the mid-plane and contours of the y-component of vorticity (ω_y) in that plane for 10 phases during one period of floor oscillation (left and middle columns, respectively). DPIV data in this plane are intrinsically more noisy than measurements in the cross-sectional ($z = 0$) plane due to weaker particle correlation that results from out-of-plane motion. The data in the $y = 0.5$ plane are cropped near the sidewalls at $x = \pm \Gamma/2$ (top and bottom of each plot) due to the flow being primarily up and down the sidewalls, producing excessively noisy data. Even though the data are noisier than in the cross-sectional plane, they clearly show the formation and propagation of the cross-axis vortices, which resemble streamwise
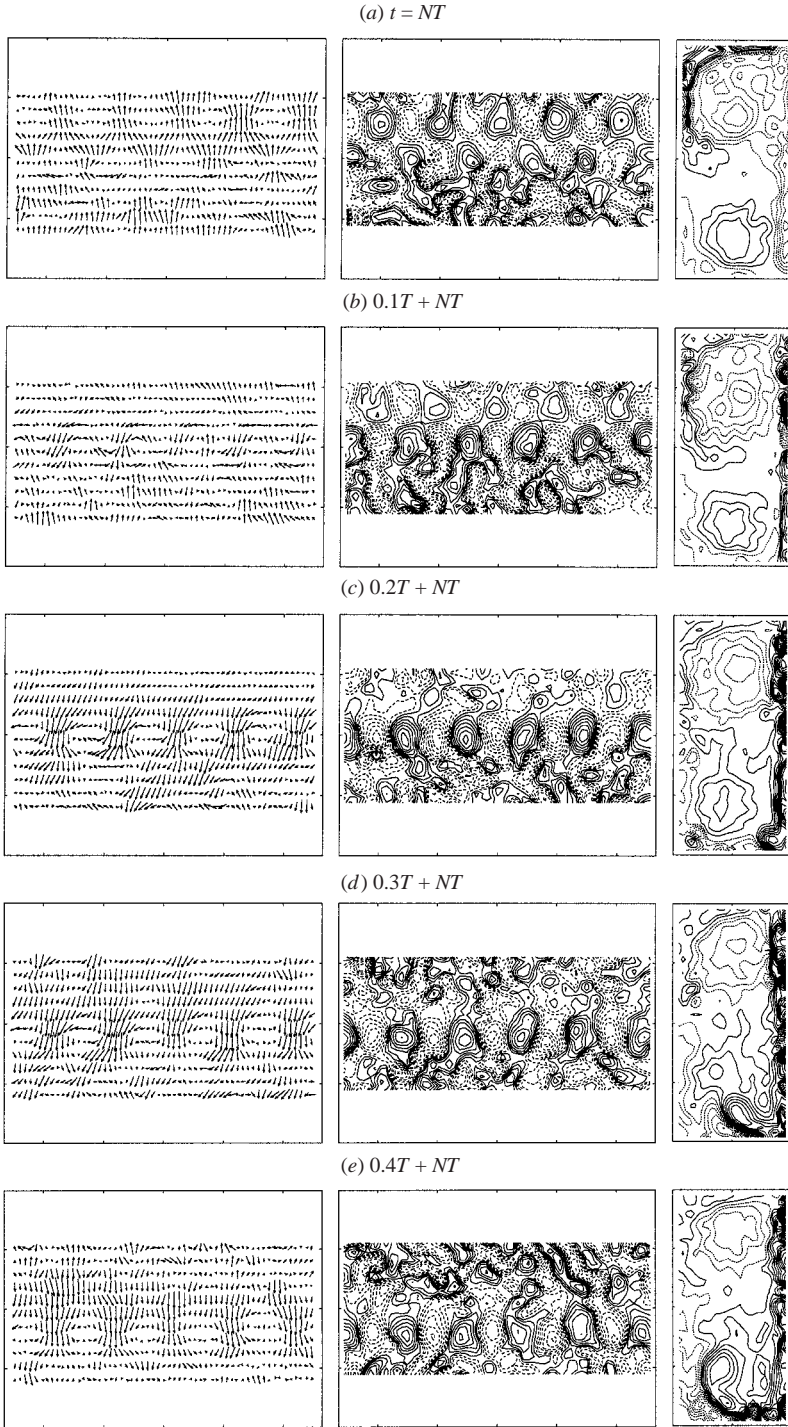
M. J. Vogel, A. H. Hirsa and J. M. Lopez

(a) $t = NT$

(b) $0.1T + NT$

(c) $0.2T + NT$

(d) $0.3T + NT$

(e) $0.4T + NT$

FIGURE 13. Experimentally measured (u, w) velocity vectors (left column), y-vorticity contours (middle column), and z-vorticity contours (right column), for ten phases over one period for flow with a rigid top at $Re = 1163$ and $St = 53$. Left and middle columns are in the $y = 0.5$ plane and show the domain $x \in [-\Gamma/2, \Gamma/2]$ and $z \in [-0.14\Lambda/2, 0.14\Lambda/2]$; the top and bottom
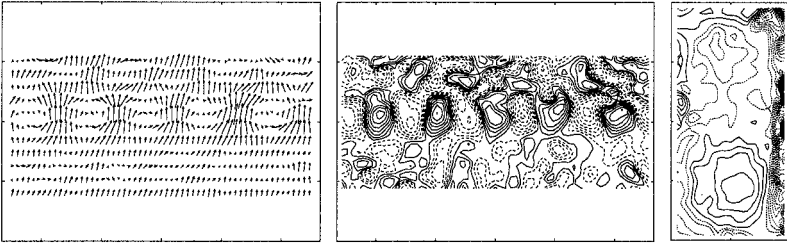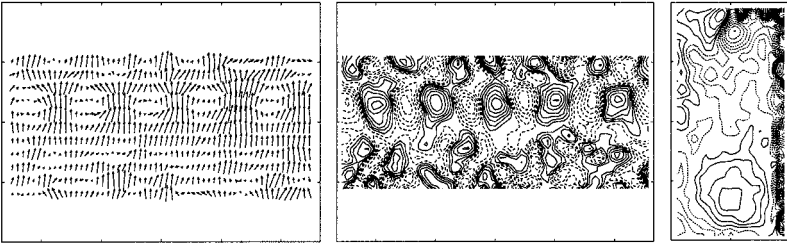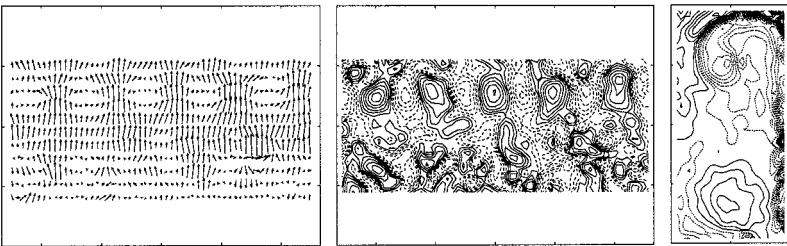
(*f*) $t = 0.5T + NT$
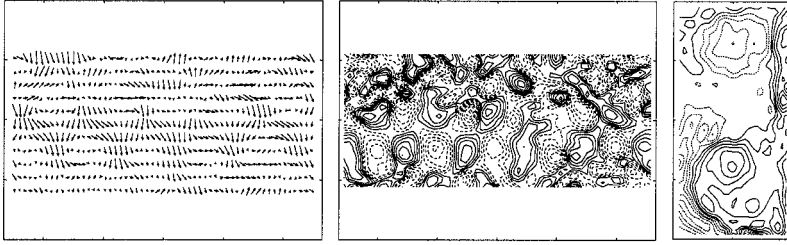
(*g*) $0.6T + NT$
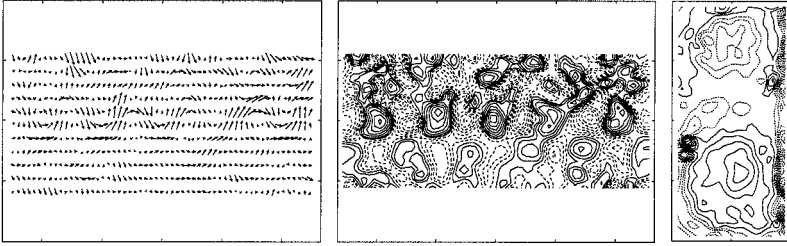
(*h*) $0.7T + NT$

(*i*) $0.8T + NT$

(*j*) $0.9T + NT$

parts of the data were cropped due to out-of-plane motion of seeding particles. The right column shows the *z*-vorticity contours in the corresponding cross-sectional plane ($z = 0$, in the domain $x \in [-\Gamma/2, \Gamma/2]$ and $y \in [0, 1]$). Measurements were taken after the start-up transients had diminished.
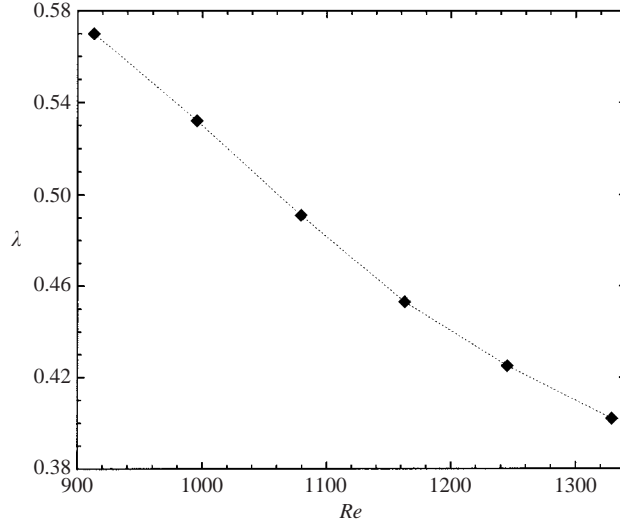
FIGURE 14. Experimentally obtained cell spacing vs. *Re*, for the rigid top case with fixed $St = 53$.

vortices (or 'braids') in mixing layers (e.g. see Bernal & Roshko 1986) and in the wake of cylinders (e.g. see Williamson 1993). Contours of z-vorticity in the cross-sectional $(z = 0)$ plane at the same phase are shown in the third column in figure 13. At $t = 0.1T + NT$, a row of counter-rotating vortices has formed at about $x = 0.01\Gamma$, which propagates downward (in the negative x-direction) with time. At $t = 0.2T + NT$, the maximum ω_y in this plane has slightly increased. By $t = 0.4T + NT$, the maximum in ω_y is located at about $x = -0.11\Gamma$, although its magnitude is reduced from the earlier phase, $t = 0.2T + NT$. At each phase, the position of the row of counter-rotating vortices can be correlated with the corresponding flow in the cross-section, in particular at the depth $y = 0.5$. The figure indicates that the counter-rotating vortices are related to the roller which is pulling the shear layer from the top wall $(y = 1)$ and appear away from the core of the roller. They appear to be associated more closely with the shear layer from the wall. During the second half of the period, another row of counter-rotating vortices forms and strengthens at about $t = 0.6T + NT$ near $x = 0$ and propagates upwards (positive x-direction), reaching approximately $x = 0.12$ by $t = 0.9T + NT$. The non-dimensional wavelength of the cellular structures in the z-direction, λ, is plotted against Re for fixed $St = 53$ in figure 14, showing that λ decreases with increasing Re. It should be noted that the standard deviation of these data is small (on the order of the symbol size).

3.3. *Transition to three-dimensional irregular flow* (*rigid top*)

When Re is increased beyond about 1350 (for $St = 53$), the three-dimensional nature of the flow is not periodic in the spanwise direction as it is at lower Re, but instead flow visualization shows dye streaks that are quite irregular. Figure 15 illustrates that there is significant three-dimensionality even at the earliest time; compare figures 15(*a*) and 12(*a*). Until $t \approx 0.7T$, the three-dimensionality is somewhat regular and periodic in the spanwise direction. By $t = 0.73T$, figure 15(*d*), there is evidence of wider spacing between some of the cellular structures, and for $t > 0.9T$ there are indications of nonlinear interactions between modes of different wavelengths. The dye sheets become very irregular by the completion of the first period, and flow visualization
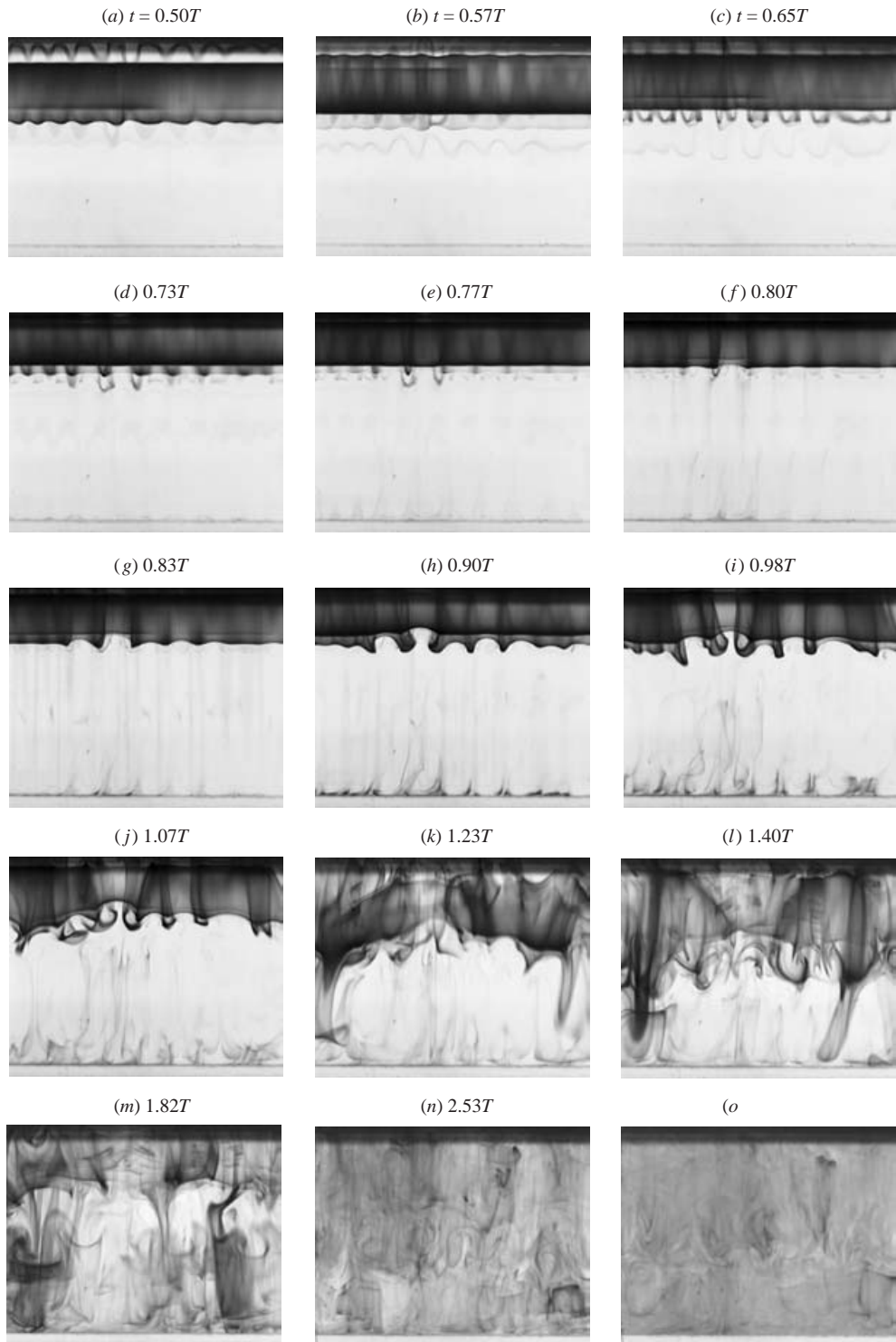
FIGURE 15. Temporal development of a three-dimensional irregular case with a rigid top at $Re = 1946$ and $St = 53$. The images were taken in the central portion of the cavity, looking from above near $z = 0$. Dye (dark) was initially injected along the sidewall seen on the bottom of the images.
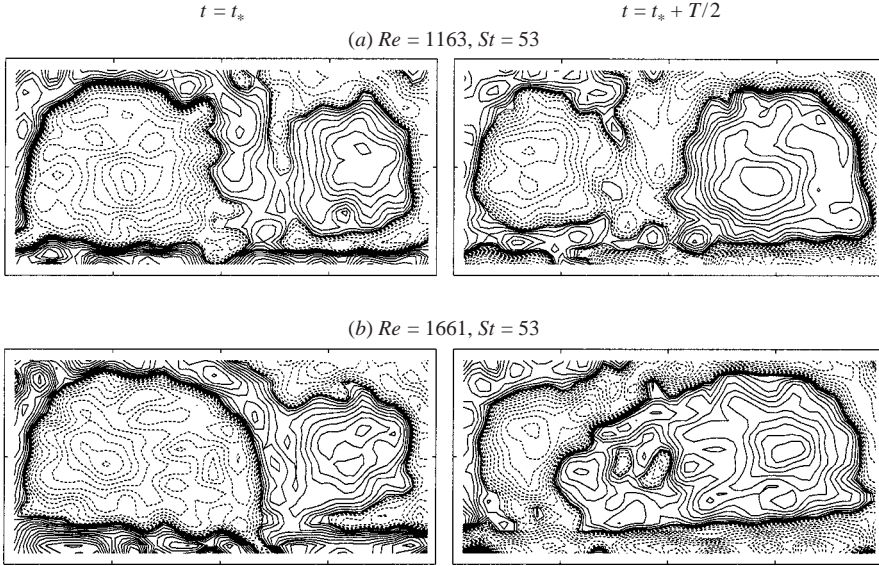
$t = t_*$ $t = t_* + T/2$

(*a*) $Re = 1163$, $St = 53$

(*b*) $Re = 1661$, $St = 53$

FIGURE 16. Contours of *z*-vorticity (from the experiment) in the $z = 0$ plane showing (*a*) a three-dimensional cellular case, and (*b*) a three-dimensional irregular case with broken *RT* symmetry. t_* is a large, arbitrary time.

is inadequate to further follow the dynamics. From the flow development at early times, it appears that the three-dimensional cellular flow that is stable for $Re < 1350$ becomes unstable to a second spanwise wavelength mode. Unfortunately, at present we do not have quantitative measures to unambiguously identify the nature of this secondary instability. Nevertheless, we have found this secondary instability to be associated with *RT*-symmetry breaking.

Figure 16 shows contours of *z*-vorticity in the cross-sectional plane $z = 0$ for (*a*) a three-dimensional cellular flow at $Re = 1163$ and (*b*) a three-dimensional irregular flow at $Re = 1661$, and their respective states half a period later. The three-dimensional cellular flow is essentially *RT* symmetric, whereas the three-dimensional irregular flow is not. It should be noted that the data in figure 16(*a*) are not as smooth as for the lower-*Re* cases (e.g. figure 6) as there is increased DPIV noise in the measurements at the larger *Re* due to increased out-of-plane motion of seeding particles caused by the three-dimensional cellular structures. Figure 16(*b*) shows that at the initial time shown, the left roller brings the shear layer from the top rigid wall to the floor in between the two rollers, whereas half a period later, the right roller brings the shear layer over the top and into the left roller. This is a clear indication of *RT*-symmetry breaking.

3.4. *Summary of the rigid top case*

The results obtained in the preceding subsections can be summarized in a stability regime diagram delineating the two-dimensional basic state, three-dimensional cellular state and three-dimensional irregular state in (St, Re)-space. This is presented in figure 17, where the transition between two-dimensional (open circles) and three-dimensional cellular states (solid squares) is emphasized. Flow states for all *St* below this transition curve are two-dimensional. The whole of (St, Re)-space was not accessible using the present apparatus (as described in §2): $St = 53$ was the
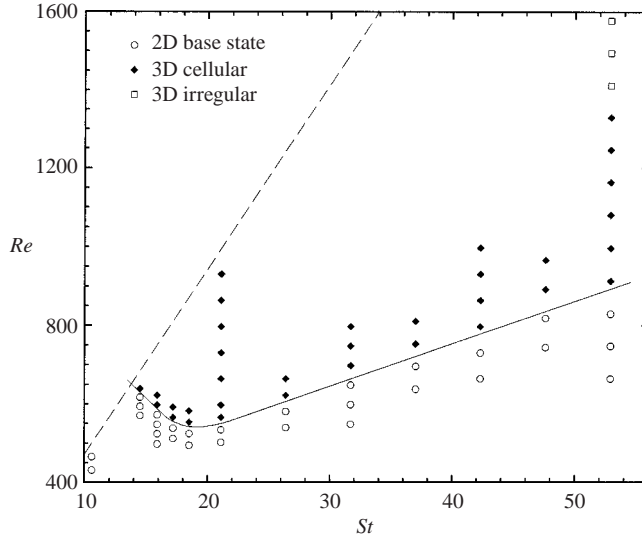
FIGURE 17. Experimentally determined stability regime diagram for the rigid top case: open circles indicate stable basic state (essentially two-dimensional, synchronous flow), solid diamonds indicate synchronous three-dimensional flow with spanwise periodic cellular structures, and open squares indicate three-dimensional irregular flow. The dashed line delineates the region in parameter space accessible with the present apparatus. Note that, as discussed in §3.5, for the free-surface case, transition Re for two-dimensional base state to three-dimensional cellular flow for $St = 20$ and 53 are the same as those shown here (to within quantization in the apparatus).

largest frequency obtainable, and the 'low-frequency' regime to the left of the dashed line was not accessible. Since the transition from three-dimensional cellular to three-dimensional irregular states is relatively ambiguous using the present techniques and not as clearly identified as the transition from two-dimensional to three-dimensional cellular flow, data were only obtained for that transition at fixed $St = 53$.

Although a direct comparison of the present measurements in the oscillatory-driven flow, i.e. non-zero St, to the steady-driven cavity is not possible due to the singular nature of the limit $St \rightarrow 0$, some observations are nevertheless noteworthy. Extrapolation of the linear relationship between Re and St for the transition between two-dimensional and three-dimensional states ($St > 20$), observed in figure 17, to $St = 0$ gives a transition Reynolds number to three dimensions of about $Re = 325$. Interestingly, this value correlates well with stability results of Albensoeder *et al.* (2001) for $\Gamma = 2$ ($\Gamma = 0.5$ according to their definition of aspect ratio) of $Re = 353$ (or 706 using their definition of Re). Furthermore, the wavelength of the three-dimensional structures also correlate with their result; extrapolation of our measurements of λ to $Re = 325$ gives $\lambda = 0.75$, which is of the same order as the wavelength reported by Albensoeder *et al.* (2001) of 1.18. The increased level of stabilization of a basic state to centrifugal instability due to periodic forcing (from a critical $Re \approx 350$ without periodic forcing to $Re \approx 900$ with a forcing frequency of $St = 53$) has also been observed experimentally (Weisberg, Kevrekidis & Smits 1997) and predicted theoretically (Marques & Lopez 1997, 2000) in a Taylor–Couette flow where the rotating inner cylinder also oscillates harmonically in the axial direction. In that case as well, the centrifugal instability of the basic state has been postponed to a Reynolds number up to twice that for instability in the unforced system.
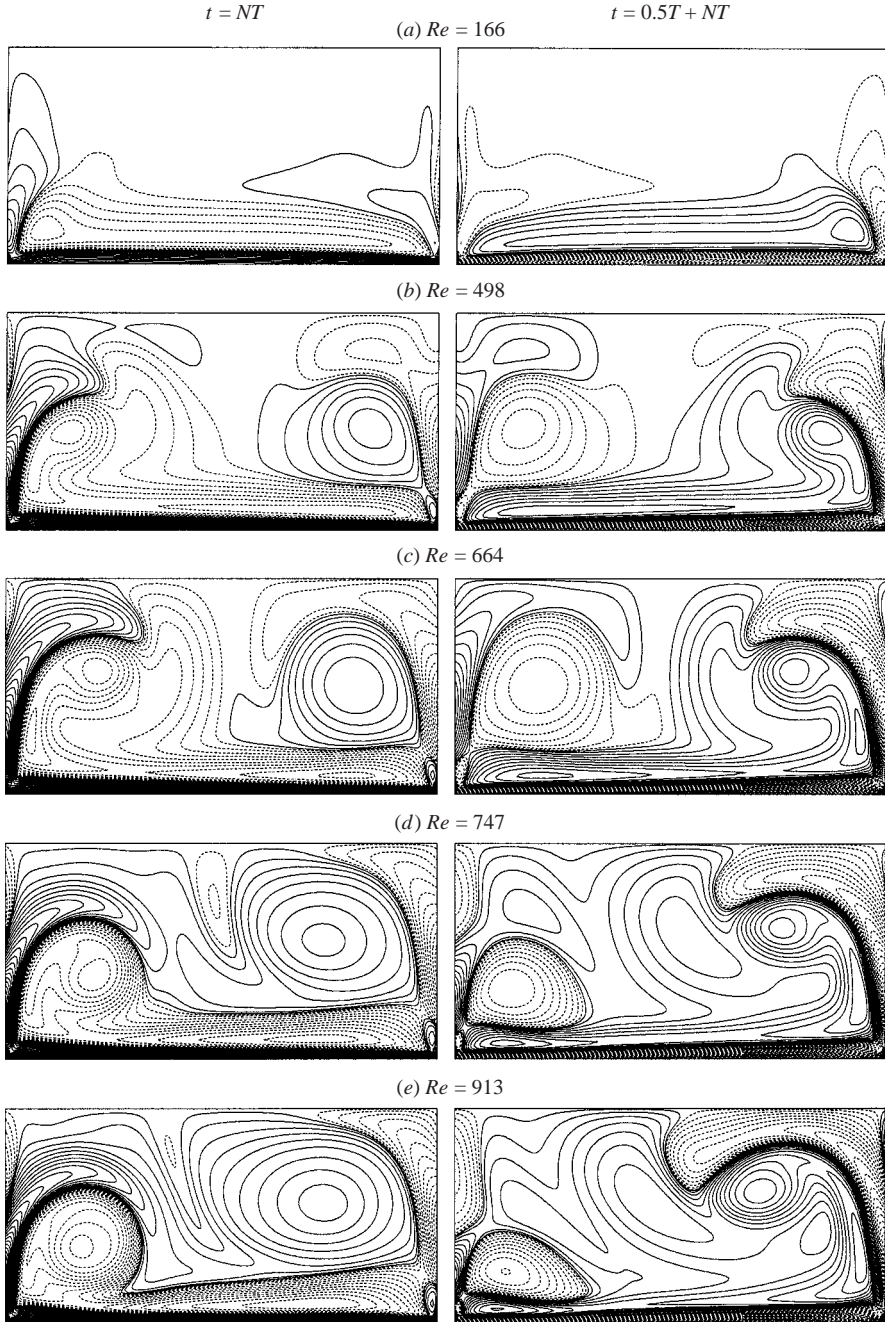
$t = NT$ $t = 0.5T + NT$

(*a*) $Re = 166$

(*b*) $Re = 498$

(*c*) $Re = 664$

(*d*) $Re = 747$

(*e*) $Re = 913$

FIGURE 18. Two-dimensional computations of z-vorticity at various Re with fixed $St = 53$ for the free-surface case. The computations show that RT-symmetry breaking occurs in the range $664 < Re < 747$. Results are shown after the start-up transients had diminished following N periods (where N is a large integer).

Similarities in the three-dimensional structures between this flow and the wake of a cylinder are not surprising, given that the symmetries of the two-dimensional periodically shedding wake are the same as those of the basic two-dimensional

$t = NT$ (*a*) $Re = 166$ $t = 0.5T + NT$

(*b*) $Re = 498$

(*c*) $Re = 664$

(*d*) $Re = 747$
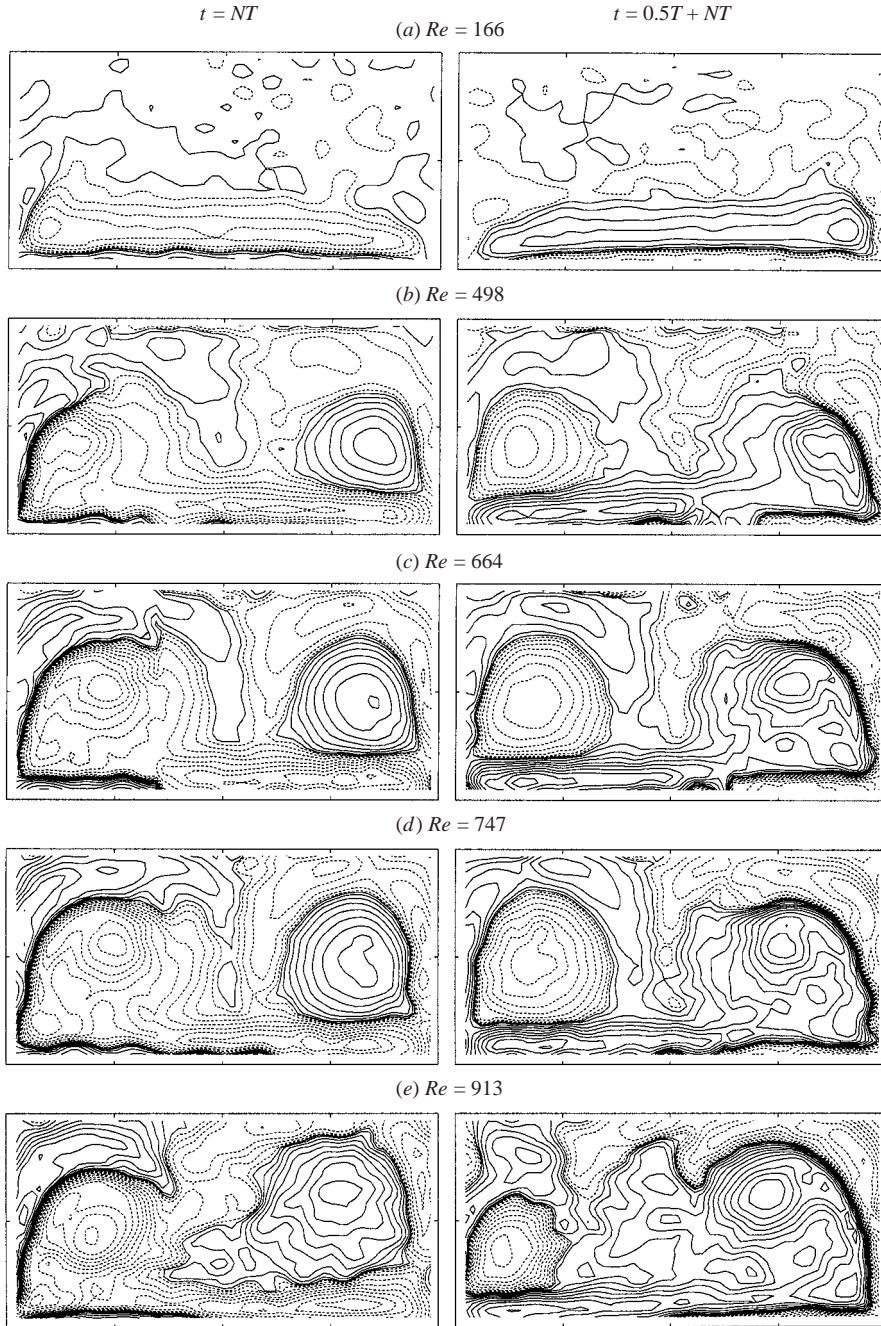
(*e*) $Re = 913$

FIGURE 19. Measurements of *z*-vorticity at various *Re* with fixed $St = 53$ for the free-surface case. The measurements show that RT-symmetry breaking occurs in the range $747 < Re < 913$. Measurements were taken after the start-up transients had diminished following N periods (where N is a large integer).

periodically driven cavity; both have the same spatial symmetry in the spanwise (z) direction, and both have the RT symmetry in the streamwise (x) direction (see discussion at the beginning of §3). In particular, the three-dimensional cellular

structures observed with the rigid top appear similar to the type-B mode of flow identified in wakes of circular cylinders (Williamson 1993; Barkley & Henderson 1996; Barkley, Tuckerman & Golubitsky 2000), consisting of cross-axis vorticity organized into braids on top of the main rollers.

3.5. *Comparisons with the free-surface case*

Since the top boundary condition can have a significant influence not only on the flow in the vicinity of the top boundary but also on the bulk flow, calculations and experiments were performed in the periodically driven cavity with a free surface. Unlike the rigid top, at the free surface the z- and x-vorticity components vanish (stress-free) while y-vorticity may be non-zero (but vanishes for the no-slip rigid top), so a number of differences between the two cases are to be expected in the two-dimensional base flow as well as the three-dimensional flows. Flow studies for the free-surface case are of particular interest due to the application of this flow as a surface viscometer (Lopez & Hirsa 2001).

The computations in figure 18 show that as Re is increased above 166, rollers form on each side. As Re is further increased, one roller eventually dominates (in this case the right roller, due to the initial direction of floor motion) over the entire period. The breaking of RT symmetry, observed in the computations, occurs as z-vorticity from the dominant roller approaches the free surface, displacing the secondary vorticity generated at the (right) wall away from the free surface. At the same time, the smaller roller (left) is pushed down by the dominant roller towards the oscillatory floor, where it tends to pump secondary vorticity from the (left) wall into the interior (i.e. toward $x = 0$). The action of this wall vorticity is to strengthen the dominant roller and move it closer to the free surface. Subsequently, the interaction of the dominant roller with the free surface induces a motion towards the interior of the cavity, which reinforces the (right) dominant roller. The interaction of the dominant roller is stronger with the free surface than the floor due to its closer proximity to the free surface. At the same time, the smaller roller (left) is closer to the floor and interacts more strongly with the floor, which causes it to travel away from the cavity centre (i.e. toward $x = -\Gamma/2$). A similar process does not occur in the rigid top case, due to the vorticity in the top wall boundary layer.

The corresponding measurements are presented in figure 19. It should be noted that the magnitude of free-surface deformation is small, which makes comparisons to calculations with a flat free surface relevant. The maximum free-surface deformation measured via surface elevation mapping (Hirsa, Vogel & Gayton 2001*b*) was found to be $50 \pm 10\,\mu\text{m}$ (Vogel 2002), which is less than 0.5% of the channel depth and half of the node spacing used for the computations. The data show that rollers form for Re above 166. However, the distribution of vorticity near the free surface is different from the computations for a stress-free interface for $Re \geqslant 498$, presented in figure 18. At higher Re, some vorticity appears at the surface, indicative of residual free-surface contamination producing surface stresses in the experiment. This boundary layer at the free surface, albeit weak compared to the rigid top case, prevents either roller from approaching the surface closely, and so one roller does not get the opportunity to dominate the other roller as in the stress-free computations. At larger $Re = 913$ (figure 19*e*), measurements show RT-symmetry breaking; the rigid top case at this (St, Re) value also showed a transition to three-dimensional flow. Here, with the free surface, the flow is three-dimensional. This RT-symmetry breaking observed in the experiments is qualitatively different from that in the (two-dimensional) computations and is a manifestation of three-dimensional flow, as discussed below. The extent to
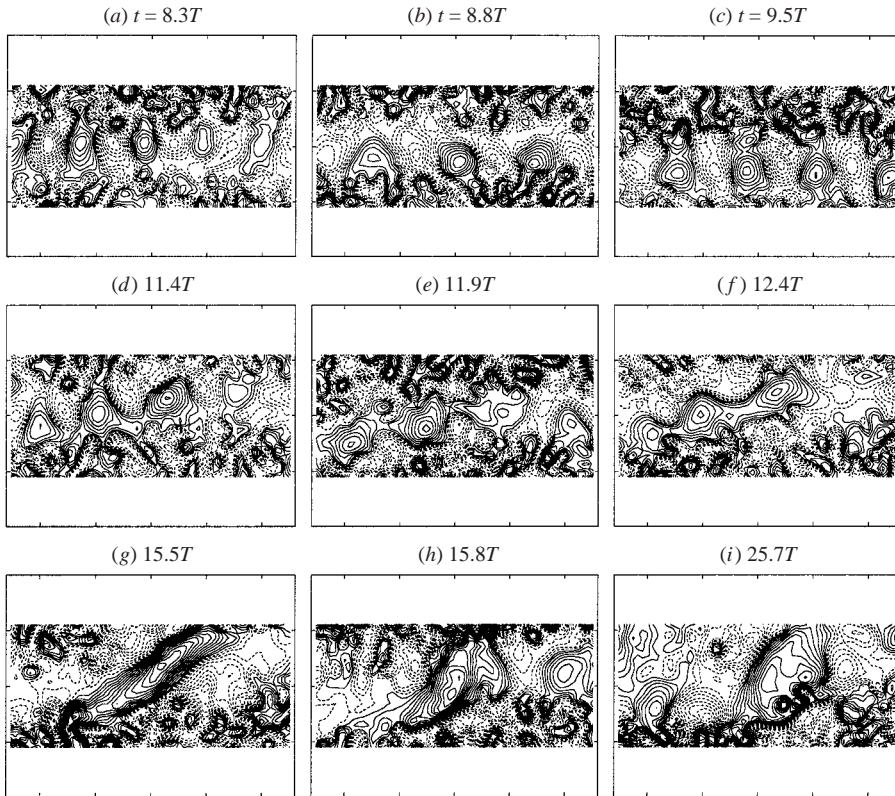
(*a*) *t* = 8.3*T*   (*b*) *t* = 8.8*T*   (*c*) *t* = 9.5*T*

(*d*) 11.4*T*   (*e*) 11.9*T*   (*f*) 12.4*T*

(*g*) 15.5*T*   (*h*) 15.8*T*   (*i*) 25.7*T*

FIGURE 20. Experimentally measured y-vorticity contours showing the temporal development of the cross-axis vortices in the (x, z)-plane at mid-depth ($y = 0.5$) for $x \in [-\Gamma/2, \Gamma/2]$ and $z \in [-0.14\Lambda/2, 0.14\Lambda/2]$, for the free-surface case at $Re = 996$ and $St = 53$. The top and bottom parts of the data were cropped due to out-of-plane motion of seeding particles.

which the lack of RT-symmetry breaking in the experiments at $Re = 747$ is due to residual vorticity at the interface (e.g. compare figures 18d and 19d) is unknown. The stabilizing effect of residual surfactants is consistent with the boundary layer generated at the free surface which can be of the same magnitude as that at a solid wall (Lopez & Hirsa 2000).

The role of residual surfactants in this system remains an open question. The presence of residual surfactants in the free-surface experiments is unavoidable with air–water systems (Scott 1975). Despite the elaborate seeding particle cleaning procedure (Hirsa *et al.* 2001*a*), the major source of free-surface contamination is still residual surfactants on the seeding particles, which are necessary for the present flow measurement technique.

Representative DPIV measurements of y-vorticity in the (x, z)-plane at mid-depth ($y = 0.5$) for a free-surface case at $Re = 996$ and $St = 53$ are shown in figure 20 at various times. At $t = 8.3T$, the figure shows a well-developed row of counter-rotating vortices near $x = 0$, similar to the three-dimensional structures found for the rigid top case (see figure 13). However, unlike the rigid top case, where the spacing of the cross-axis vortices remained essentially constant, the vortices in the free-surface case have qualitatively different behaviour. Half a period later ($t = 8.8T$), the figure also shows a single row of counter-rotating vortices, but with a markedly larger spacing

than at the earlier time. The different rows of cross-axis vortices observed at these two times appear to be independent of each other and each one corresponds to a main roller, similar to the rigid top case. One period later ($t = 9.5T$), there is evidence of merging of the two separate rows into a single row, as the vortices no longer appear and disappear during each period. The structures are now somewhat elongated in the x-direction. Unlike the rigid top case, where two distinct rows of cross-axis vortices appeared and disappeared with their corresponding rollers indefinitely, for the free-surface case a single row of vortices persists after $t = 9T$. The rollers continue to periodically feed this single row of vortices as they develop. About two periods later ($t = 11.4T$), the cross-axis vortices no longer reside on a straight line. Furthermore, the data show evidence of similar-signed vortices merging. At later times ($t > 13T$), the growth and development of a single dominant structure (positive y-vorticity) is visible near the centre. The last frame of the figure, obtained many periods later, shows the fully developed state of the cross-axis structures.

The temporal development of y-vorticity as seen in the mid-depth plane ($y = 0.5$) is shown schematically over a larger field of view in figure 21. At early times, as shown in frame (*a*), no cross-axis vorticity is present (as in the rigid top case). Rows of time-periodic small cells subsequently develop, as depicted in frame (*b*), that are associated with the main rollers, similar to the rigid top case. However, the development time to this stage is much longer (six to eight periods) than for the rigid top (three to four periods). A short time later, the two rows of cells have merged to become one persistent row, and the line that the row lies on begins to curve, as shown in frame (*c*). The cells of like-signed vorticity then slowly merge and form the elongated structures shown in frame (*d*). Finally, the elongated structures are tilted to their final position shown in frame (*e*). It should be noted that the faint curve that the vorticity lies on oscillates slightly in the x-direction during a period of flow with the forcing motion, as was seen for the moving rows of cells in figure 13. The distribution of y-vorticity appears to be consistent with RT-symmetry breaking that was experimentally observed in the (x, y) cross-sectional plane (see figure 16*b*). Simultaneously observing cross-sections of the flow at different z-locations has revealed a variety of flow features: at certain z-locations, the left roller is dominant, while at other locations the right roller is dominant. At other locations, the flow still appears symmetric. These different states appear to be periodic in the z-direction (left roller dominant, symmetric, right roller dominant, symmetric, and so on). The wavelength of this periodicity seems to be the same as the wavelength of the cells shown in figure 21(*e*), implying that areas of concentrated y-vorticity interact with the main rollers and prevent them from rising to the free surface. This sinusoidal deformation of the axis of the main rollers is reminiscent of the deformation of the shed rollers in the wake of cylinders when the three-dimensional mode is of type-A (Williamson 1993; Brede, Eckelmann & Rockwell 1996; Robichaux, Balachandar & Vanka 1999).

Measurements in horizontal planes at $y > 0.5$, including the free surface, show development of y-vorticity similar to that at $y = 0.5$. The one main difference between the distributions at $y = 0.5$ and $y = 1$ is that at the free surface, only the larger, elongated structures are apparent. So, the development sequence at the surface is also represented by figure 21, except that stages (*b*) and (*c*) are not observed. This provides clear evidence that the elongated structures extend from the bulk and terminate at the free surface. Free-surface kinematics require normal termination of vortex lines (Lugt 1987), and this may be related to the absence of smaller structures at the free surface which are present at intermediate times at $y = 0.5$.
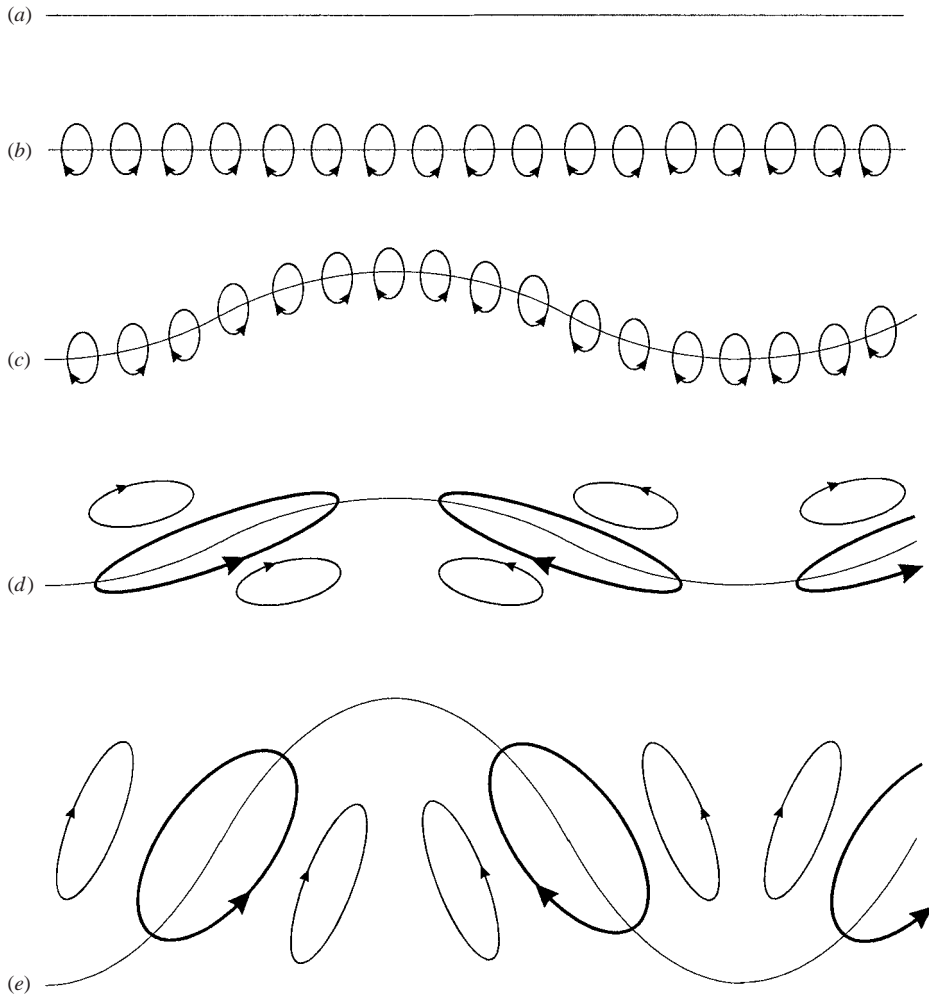
FIGURE 21. Schematic of the temporal development of cross-axis structures for the free-surface case as seen in the mid-plane ($y = 0.5$). The behaviour in the plane of the free surface ($y = 1$), is similar, except that stages (b) and (c) are not observed.

Finally, the measurements for the free-surface case can be summarized on the same stability diagram as the rigid top case. Although fewer experiments were conducted with the free surface (only for $St = 20$ and 53), the transition from the two-dimensional base state to three-dimensional cellular flow was found to agree with the stability behaviour depicted in figure 17, to within the quantization limits of Re and St. The major difference between the two cases is the nature of the three-dimensional flow following instability of the two-dimensional flow.

4. Conclusions

The primary motivation for this study was to determine if the flow in a periodically driven oscillatory cavity could be described as essentially two-dimensional (i.e. independent of the spanwise direction) in some region of (St, Re)-parameter space, and if so, to determine the bounds of that region. By conducting experiments using flow visualization and DPIV measurements in a cavity of ratio 1:2:19 and comparing

the observations and measurements with two-dimensional computations, we have established the bounds for which the flow is essentially two-dimensional for the two cases of a rigid top and a free surface. The viability of this flow as a surface viscometer, as was first suggested in Lopez & Hirsa (2001) where the theory was based on two-dimensional flow, is borne out by the present study. In fact, they established that the flow would be sensitive to surface viscosity at $Re = 100$ and $St = 16$; it is seen here that Re and St can be substantially increased without the flow losing stability to three-dimensional disturbances. Thus, its operational range as a surface viscometer is considerably larger than originally anticipated based on results for the steady-driven cavity flow, and hence it is now expected to have improved signal-to-noise ratios.

Beyond establishing its utility as a surface viscometer, the nature of the onset of three-dimensional flow was investigated. Although such a study for this flow has not been previously presented, the dynamics at work are common to other well-studied flows with the same symmetry group, and these connections have been explored. The space–time symmetry of the periodically driven cavity is also common to the wake of a cylinder following the Hopf bifurcation to periodic shedding. Such analogies between the periodically driven cavity and other flows that are geometrically very different have been found.

Due to the mechanical constraints of the experimental apparatus, which limit the range of parameters that could be explored and do not allow for their continuous variation, a number of open questions remain concerning the sequence of bifurcations and the symmetry of the resulting flow states as the parameters are varied. These will be investigated using Floquet analysis of the periodic two-dimensional base state and full nonlinear three-dimensional computations that will be reported elsewhere.

Appendix

The basic two-dimensional state is computed using a second-order finite-difference scheme together with a predictor–corrector time integration. The two-dimensional Navier–Stokes equations are cast in streamfunction–vorticity form, and non-dimensionalized using the same scalings as described in §2. We write the two-dimensional velocity $(u, v) = (\psi_y, -\psi_x)$, where ψ is the streamfunction, and the z-vorticity is

$$\eta = -\psi_{xx} - \psi_{yy}. \tag{A 1}$$

The two-dimensional Navier–Stokes equations reduce to an evolution equation for η:

$$\eta_t + \psi_y \eta_x - \psi_x \eta_y = \eta_{xx} + \eta_{yy}, \tag{A 2}$$

with boundary conditions $\psi(\pm\Gamma, y, t) = \psi_x(\pm\Gamma, y, t) = 0$, and $\eta(\pm\Gamma, y, t) = -\psi_{xx}(\pm\Gamma, y, t)$; $\psi(x, 0, t) = 0$, $\psi_y(x, 0, t) = Re\sin(2\pi St\, t)$, and $\eta(x, 0, t) = -\psi_{yy}(x, 0, t)$. When the top ($y = 1$) is rigid no-slip, then $\psi(x, 1, t) = \psi_y(x, 1, t) = 0$, and $\eta(x, 1, t) = -\psi_{yy}(x, 1, t)$; and when the top is stress-free then $\psi(x, 1, t) = \eta(x, 1, t) = 0$.

For all the cases considered in this paper, 101 grid points in z and 201 grid points in x have been used. This was more than adequate spatial resolution: halving the number of grid points in each direction resulted in negligible changes in the solutions. For the temporal evolution, 1000 times steps per floor oscillation period when $St \sim 50$ and 2000 time steps per period for $St \in (20, 40)$ were used; the lower frequency

cases require more steps per period for numerical stability. The predictor–corrector scheme is essentially a two-stage second-order Runge–Kutta method, where ψ and the boundary conditions on η are evaluated at each stage. η is advanced explicitly according to the discrete version of (A 2), and ψ is determined at each stage by solving (A 1). Equation (A 1) is solved by diagonalizing in the x-direction, leading to a system of one-dimensional tridiagonal equations in the y-direction, which can be very efficiently solved in parallel. Typically, following a start from rest, transients decay within about 10 to 20 floor oscillation periods.

REFERENCES

ALBENSOEDER, S., KUHLMANN, H. C. & RATH, H. J. 2001 Three-dimensional centrifugal-flow instabilities in the lid-driven cavity problem. *Phys. Fluids* **13**, 121–135.

BAGNOLD, R. A. 1946 Motion of waves in shallow water: Interaction of waves and sand bottom. *Proc. R. Soc. Lond.* A **187**, 1–15.

BARKLEY, D. & HENDERSON, R. D. 1996 Three-dimensional Floquet stability analysis of the wake of a circular cylinder. *J. Fluid Mech.* **322**, 215–241.

BARKLEY, D., TUCKERMAN, L. S. & GOLUBITSKY, M. 2000 Bifurcation theory for three-dimensional flow in the wake of a circular cylinder. *Phys. Rev.* E **61**, 5247–5252.

BENJAMIN, T. B. 1978 Bifurcation phenomena in steady flows of a viscous fluid. *Proc. R. Soc. Lond.* A **359**, 1–26.

BERNAL, L. P. & ROSHKO, A. 1986 Streamwise vortex structure in plane mixing layers. *J. Fluid Mech.* **170**, 499–525.

BREDE, M., ECKELMANN, H. & ROCKWELL, D. 1996 On secondary vortices in the cylinder wake. *Phys. Fluids* **8**, 2117–2124.

CHOSSAT, P. & IOOSS, G. 1994 *The Couette–Taylor Problem.* Springer.

CHOSSAT, P. & LAUTERBACH, R. 2000 *Methods in Equivariant Bifurcations and Dynamical Systems.* World Scientific.

GOLUBITSKY, M., STEWART, I. & SCHAEFFER, D. G. 1988 *Singularities and Groups in Bifurcation Theory. Volume II.* Springer.

GUERMOND, J.-L., MIGEON, C., PINEAU, G. & QUARTAPELLE, L. 2002 Start-up flows in a three-dimensional rectangular driven cavity of aspect ratio 1:1:2 at $Re = 1000$. *J. Fluid Mech.* **450**, 169–199.

HAMA, F. R. 1962 Streaklines in a perturbed shear flow. *Phys. Fluids* **5**, 644–650.

HIRSA, A. H., LOPEZ, J. M. & MIRAGHAIE, R. 2001a Measurement and computation of hydrodynamic coupling at an air/water interface in the presence of an insoluble monolayer. *J. Fluid Mech.* **443**, 271–292.

HIRSA, A., VOGEL, M. J. & GAYTON, J. D. 2001b Digital particle velocimetry technique for free-surface boundary layer measurements: Application to vortex pair interactions. *Exps. Fluids* **31**, 127–139.

JONSSON, I. G. 1980 A new approach to oscillatory rough turbulent boundary layers. *Ocean Engng* **7**, 109–152.

VON KERCZEK, C. & DAVIS, S. H. 1972 Stability of oscillatory Stokes layers. *Stud. Appl. Maths* **51**, 239–252.

VON KERCZEK, C. & DAVIS, S. H. 1974 Linear stability of oscillatory Stokes layers. *J. Fluid Mech.* **62**, 753–773.

KIM, J. & MOIN, P. 1985 Application of a fractional step method to incompressible Navier-Stokes equations. *J. Comput. Phys.* **59**, 308–323.

KRSTIC, R. V. & FERNANDO, H. J. S. 2001 The nature of rough-wall oscillatory boundary layers. *J. Hydraul. Res.* **39**, 655–666.

KUZNETSOV, Y. A. 1998 *Elements of Applied Bifurcation Theory*, 2nd edn. Springer.

LAMB, J. S. W. & MELBOURNE, I. 1999a Bifurcation from discrete rotating waves. *Arch. Rat. Mech. Anal.* **149**, 229–270.

LAMB, J. S. W. & MELBOURNE, I. 1999b Bifurcation from periodic solutions with spatiotemporal symmetry. In *Pattern Formation in Continuous and Coupled Systems* (ed. M. Golubitsky,

　　　D. Luss & S. Strogatz). IMA Volumes in Mathematics and its Applications, vol. 115,
　　　pp. 175–191. Springer.

Lopez, J. M. & Hirsa, A. 2000 Surfactant influenced gas/liquid interfaces: Nonlinear equation of
　　　state and finite surface viscosities. *J. Colloid Interface Sci.* **229**, 575–583.

Lopez, J. M. & Hirsa, A. 2001 Oscillatory driven cavity with an air/water interface and an insoluble
　　　monolayer: Surface viscosity effects. *J. Colloid Interface Sci.* **242**, 1–5.

Lugt, H. J. 1987 Local flow properties at a viscous free-surface. *Phys. Fluids* **30**, 3647–3652.

Marques, F. & Lopez, J. M. 1997 Taylor–Couette flow with axial oscillations of the inner cylinder:
　　　Floquet analysis of the basic flow. *J. Fluid Mech.* **348**, 153–175.

Marques, F. & Lopez, J. M. 2000 Spatial and temporal resonances in a periodically forced extended
　　　system. *Physica* D **136**, 340–352.

O'Brien, V. 1975a Unsteady cavity flows: Oscillatory flat box flows. *J. Appl. Mech.* **42**, 557–563.

O'Brien, V. 1975b Unsteady separation phenomena in a two-dimensional cavity. *AIAA J.* **13**,
　　　415–416.

Ottino, J. M. 1997 *The Kinematics of Mixing: Stretching, Chaos, and Transport.* Cambridge
　　　University Press.

Ramanan, N. & Homsy, G. M. 1994 Linear stability of lid-driven cavity flow. *Phys. Fluids* **6**,
　　　2690–2701.

Rhee, H. S., Koseff, J. R. & Street, R. L. 1984 Flow visualization of recirculating flow by
　　　rheoscopic liquid and liquid crystal technique. *Exps. Fluids* **2**, 57–64.

Robichaux, J., Balachandar, S. & Vanka, S. P. 1999 Three-dimensional Floquet instability of the
　　　wake of square cylinder. *Phys. Fluids* **11**, 560–578.

Scott, J. C. 1975 The preparation of water for surface-clean fluid mechanics. *J. Fluid Mech.* **69**,
　　　339–351.

Shankar, P. N. & Deshpande, M. D. 2000 Fluid mechanics in the driven cavity. *Annu. Rev. Fluid
　　　Mech.* **32**, 93–136.

Sleath, J. F. A. 1987 Turbulent oscillatory flow over rough beds. *J. Fluid Mech.* **182**, 369–409.

Stokes, G. G. 1851 On the effect of the internal friction of fluids on the motion of pendulums.
　　　Trans. Camb. Phil. Soc. **9**, 8.

Swift, J. W. & Wiesenfeld, K. 1984 Suppression of period doubling in symmetric systems. *Phys.
　　　Rev. Lett.* **52**, 705–708.

Vogel, M. J. 2002 Measurements of monolayer hydrodynamics at an air/water interface. PhD
　　　thesis, Department of Mechanical Engineering, Rensselaer Polytechnic Institute.

Weisberg, A. Y., Kevrekidis, I. G. & Smits, A. J. 1997 Delaying transition in Taylor–Couette flow
　　　with axial motion of the inner cylinder. *J. Fluid Mech.* **348**, 141–151.

Williamson, C. H. K. 1993 The natural and forced formation of spot-like 'vortex dislocations' in
　　　the transition of a wake. *J. Fluid Mech.* **243**, 393–441.